

Air Force Institute of Technology

AFIT Scholar

Theses and Dissertations

Student Graduate Works

6-6-2006

Characterization of Passivated Indium Antimonide

Catherine Ann Taylor

Follow this and additional works at: <https://scholar.afit.edu/etd>



Part of the [Semiconductor and Optical Materials Commons](#)

Recommended Citation

Taylor, Catherine Ann, "Characterization of Passivated Indium Antimonide" (2006). *Theses and Dissertations*. 3368.

<https://scholar.afit.edu/etd/3368>

This Thesis is brought to you for free and open access by the Student Graduate Works at AFIT Scholar. It has been accepted for inclusion in Theses and Dissertations by an authorized administrator of AFIT Scholar. For more information, please contact AFIT.ENWL.Repository@us.af.mil.



CHARACTERIZATION OF PASSIVATED INDIUM ANTIMONIDE

THESIS

Catherine Ann Taylor, BS, MS, Civilian

AFIT/GEO/ENP/06-03

**DEPARTMENT OF THE AIR FORCE
AIR UNIVERSITY**

AIR FORCE INSTITUTE OF TECHNOLOGY

Wright-Patterson Air Force Base, Ohio

APPROVED FOR PUBLIC RELEASE; DISTRIBUTION UNLIMITED

The views expressed in this thesis are those of the author and do not reflect the official policy or position of the United States Air Force, Department of Defense, or the United States Government.

AFIT/GEO/ENP/06-03

CHARACTERIZATION OF PASSIVATED INDIUM ANTIMONIDE

THESIS

Presented to the Faculty

Department of Engineering Physics

Graduate School of Engineering and Management

Air Force Institute of Technology

Air University

Air Education and Training Command

In Partial Fulfillment of the Requirements for the

Degree of Master of Science (Electro Optics)

Catherine Ann Taylor, BS, MS

Civilian

June 2006

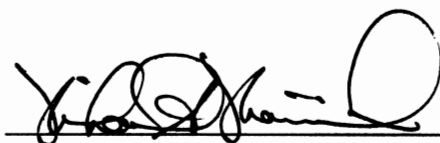
APPROVED FOR PUBLIC RELEASE; DISTRIBUTION UNLIMITED

CHARACTERIZATION OF PASSIVATED INDIUM ANTIMONIDE

Catherine Ann Taylor, BS, MS

Civilian

Approved:



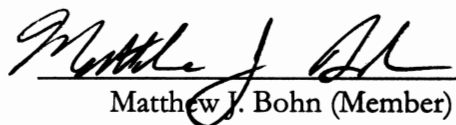
Michael A. Marciniak (Chairman)

6 Jun 06
date



Robert L. Hengehold (Member)

6 Jun 06
date



Matthew J. Bohn (Member)

6/6/06
date

Abstract

Infrared absorption and photoluminescence measurements have been used to optically characterize bulk-grown, 680- μm thick, indium antimonide (InSb), both as-grown and after passivation by either anodization or a 700- \AA layer of silicon oxide (SiO_x). Spectra were obtained using Fourier transform infrared (FT-IR) spectroscopy. Results include the effects of sample temperature in the range of 10 to 300 K and 4.636- μm laser pump power in the range of 28 mW to 1.43 W for the photoluminescence spectrum.

AFTT/GEO/ENP/06-03

Mattheo

Acknowledgments

I would like to thank Mike Garter of L3 Communications: Cincinnati Electronics for supplying the InSb samples used in this study. I gratefully acknowledge the technical support from Mike Ranft and Greg Smith and the assistance of John Callahan. Thanks to Tim Cooper, AFRL/MLPS, for performing Hall measurements. I also give my sincerest thanks to Beth Moore for lending the occasional helping hand. Finally, I wish to express gratitude to my advisor, Mike Marciniak.

Catherine Ann Taylor

Table of Contents

	Page
Abstract.....	iv
Acknowledgments	vi
List of Figures	ix
List of Tables.....	xii
I. Introduction.....	1
1.1 Background	1
1.2 Characterization Techniques	2
1.3 Research Objectives.....	4
II. Theoretical Background	7
2.1 Chapter Overview	7
2.2 Semiconductor Characteristics	7
2.3 Absorption and Emission of Photons	21
2.4 Relevant Research	27
2.5 Summary.....	31
III. Experimental Methods.....	33
3.1 Chapter Overview	33
3.2 Sample Preparation	33
3.3 Cryogenic System.....	34
3.4 FT-IR Spectroscopy.....	37
3.5 Summary.....	42
IV. Results and Discussion	43
4.1 Chapter Overview	43
4.2 Absorption	43
4.3 Photoluminescence	52
4.4 Variable Temperature Hall Measurements	60
4.5 Summary.....	69
V. Conclusions	70
5.1 Conclusions of Research.....	70
5.2 Significance of Research.....	70
5.3 Recommendations for Future Research	70

	Page
Bibliography	72

List of Figures

Figure	Page
2.1. Crystalline structure unit cells. (a) simple cubic; (b) face centered cubic; (c) diamond; (d) zincblende (Sze 1981:8).....	9
2.2. Tetrahedral Bonding (Sze 2002: 27).....	9
2.3. Coulomb potential and its eigenstates (Eisberg & Resnick 1985:239).....	11
2.4. Eigenstate splitting due to interactions with nearby atoms (Eisberg & Resnick 1985:447).....	12
2.5. Energy band formation as atoms are brought closer together in a diamond lattice structure (Willardson & Beer 1967:197)	13
2.6. Parabolic energy band diagram. (Sze 2002:3)	15
2.7. (a) flat energy band diagram and (b) corresponding density of states, (c) Fermi distribution function, and (d) carrier concentrations. (Sze 1981: 23)	18
2.8. Absorptive transistions. (a) band to band; (b) valence band to donor state; (c) donor to conduction band; (d) acceptor to conduction band; (e) valence band to acceptor level; (f) acceptor level to donor level.....	26
2.9. Temperature dependence of bandgap energy for InSb as defined in Equation (37).....	29
2.10. Rowell's (1988:40) photoluminescence spectra. (a) photoluminescence spectra of InSb with varying temperatures and 67 mW pump power. (b) photoluminescence spectra of InSb with varying pump power at 5.1 K.	30
3.1. Cross view of wafers and their layers.....	33
3.2. Helitran open cycle cryogenic refrigeration system. (ARS 2001).....	35
3.3. Transmission spectrum of zinc selenide windows (Del Mar Ventures 2006).....	36
3.4. Michaelson Interferometer. The beams are displaced for clarity. (Adapted from Bio-Rad Laboratories 1992)	37
3.5. Noise test of Bio-Rad scans to co-add.	39
3.6. Set-up for photoluminescence experiments.	40
4.1. Absorptance near the edge and center of the bare InSb wafer at 80 K.....	44

Figure	Page
4.2. Absorption coefficient as a function of temperature for bare InSb at 300 K (\square), 160 K (\diamond), 80 K (\times), and 10 K (\circ).....	45
4.3. Comparison of theoretical absorption coefficient of bare InSb to the measured absorption coefficient at 10 K and 200 K.....	46
4.4. Absorptance of edge and center of anodized InSb wafer.....	48
4.5. Impurity absorption of anodized InSb at the center of the wafer at 300 K (\square), 280 K (\circ), 260 K (\times), and 15 K (Δ).....	49
4.6. Absorptance of edge and center of SiO_x on InSb.....	50
4.7. Impurity absorption of SiO_x -on-InSb at center of the wafer at 300 K (\square), 280 K (\circ), 260 K (\times), and 10 K (Δ).....	51
4.8. Absorptance at 80 K of InSb, anodized InSb and SiO on InSb. The dashed line is the theoretical bandgap energy.....	53
4.9. Overlay plot of photoluminescence and absorptance spectra of bare InSb at 22 K. The photoluminescence peak is at 0.232 eV. The theoretical bandgap energy is 0.234 eV.....	54
4.10. Photoluminescence of bare InSb taken at 22 K with increasing optical pump powers: 28 mW, 48 mW, and 80 mW.	56
4.11. Photoluminescence of bare InSb taken with 80 mW optical pump power at temperatures: 22 K, 24 K, and 26 K.....	57
4.12. Photoluminescence anodized InSb taken at 22 K with increasing optical pump powers: 126 mW, 354 mW, 522 mW, and 960 mW.....	58
4.13. Overlay plot of impurity peak absorptance and photoluminescence for the anodized InSb sample at 80 K.	59
4.14. Overlay plot of impurity peak absorptance and photoluminescence for the SiO_x -on-InSb sample at 80 K.	61
4.15. Photoluminescence of SiO_x -on-InSb taken at 20.5 K with increasing optical pump powers: 66 mW, 180 mW, 372 mW, 600 mW, and 1.34 W.....	62
4.16. Photoluminescence of SiO_x -on-InSb taken with an optical pump power of 1.34 W at temperatures of 20.5 K, 26 K, and 80 K.....	63

Figure	Page
4.17. Lower energy sub-peak of main photoluminescence peak of SiO _x -on-InSb. Optical pump power is 1.34 W and curves represent measurements taken at 20.5 K, 22 K, 26 K, 40 K and 80 K.	64
4.18. Higher energy sub-peak of main photoluminescence peak of SiO _x -on-InSb. Optical pump power is 1.34 W and curves represent measurements taken at 20.5 K, 22 K, 26 K 40 K and 80 K.....	65
4.19. Conductivity of InSb as a function of inverse temperature. The higher and lower temperature realms have been fitted with separate exponential curves.....	66
4.20. Conductivity of the SiO _x sample as a function of inverse temperature. The higher and lower temperature realms have been fitted with separate exponential curves.	68

List of Tables

Table	Page
1. Comparison of InSb material properties	28

CHARACTERIZATION OF PASSIVATED INDIUM ANTIMONIDE

I. Introduction

1.1 Background

Infrared (IR) radiation is light whose wavelengths range from just longer than red light (780 nm) out to the wavelengths of radio waves (about 1 mm). This range of wavelengths corresponds to an energy spectrum due to the relation,

$$E = \frac{hc}{\lambda}, \quad (1)$$

where h is Planck's constant, c is the speed of light, and λ is wavelength of light. The energy range for IR radiation is then 0.01 to 1.6 eV. This energy range is split into three other sub-regions. Near-IR includes wavelengths ranging from 0.78 to 1.5 μm . Mid-IR consists of 1.5 to 15 μm . Far-IR ranges from 15 to 1000 μm . "Infrared waves are also called heat waves because they can be detected by the observation of the increase of temperature of the object absorbing them" (Nussbaum & Phillips 1976:143).

The ability to detect an object from 'heat' waves instead of visible waves has become a key technology for the military. "Heat-seeking missiles" have a sensor capable of detecting the large IR signal given off by the hot body parts and exhaust plume of jet engines. Other applications include ground-based and space-based IR astronomy. These devices all rely on detectors that can sense radiation in the mid-IR.

There are two main types of optical detectors that work in the mid-IR: thermal detectors and photon detectors. Thermal detectors detect incident radiation and change the temperature of the detector material. The material properties, such as resistance or polarity, change and thus radiation is detected. Photon detectors have the ability to detect radiation at a rate much faster than thermal detectors. Photon detectors detect radiation by absorbing a photon which, in turn, creates an electron-hole pair. Often, photon detectors are made of semiconducting materials.

Semiconducting materials have a relatively narrow bandgap compared to insulators. Incident light in the form of photons creates electron-hole pairs, or carriers, provided that the photon energy is greater than the semiconductor's bandgap energy. These generated carriers will conduct and external circuitry collects and records the signal. The capabilities of a photon detector are strongly correlated to the materials used to make that detector. In order to improve the performance of a detector, it is necessary to understand the properties of that semiconductor.

1.2 Characterization Techniques

Semiconductor materials can be characterized using optical and electrical techniques. Electrical techniques provide information on resistivity, carrier concentration, and mobility, which after careful analysis can provide insight to activation energies and impurity levels within the bandgap. Optical diagnostics are used to characterize the properties of a medium by analyzing the optical radiation transmitted, reflected, or emitted through or by the medium. This can also lead to information on bandgaps and transition energies, but in a more direct way than electrical measurements.

There are three ways that an optical source can be used as a diagnostic tool, as mentioned above. For transmission measurements, a light source with a broad spectrum is incident upon a sample. This sample then absorbs all wavelengths corresponding to allowed energy transitions. Any wavelengths not absorbed by the sample pass through the sample and are recorded by the detector. By taking the ratios of the incident and transmitted intensities as a function of wavelength, one can conclude which wavelengths were absorbed and, hence, their corresponding energies. The intensity of the absorbed light at each energy level also gives insight to the number of transitions available and the probability the transition will occur.

Reflection works in a very similar way to transmission. A broad spectrum source is incident on a sample. However in this case, the sample is placed on an angle and all wavelengths not absorbed or transmitted by the sample are reflected and then collected by a detector. Index of refraction for a material can be determined by these measurements.

For emission measurements, and in particular photoluminescence measurements, a laser is incident upon a sample. Provided that the photon energy of the laser beam is greater than or equal to the energy gap of the sample, electrons are excited from valence states to conduction states. Excited electrons in the sample may then give off a photon to return to a more stable state. An electron excited to a higher energy state will often relax to a lower energy state in the conduction band via phonon emission. Therefore, emission typically occurs at wavelengths near the bandedge. Impurities and defects in the material can lead to emission at wavelengths or energies other than the bandgap energy.

Emitted photons are collected by a detector and emitted intensity versus wavelength is plotted.

Cooling a sample to very low temperatures is a technique used to enhance characterization of samples. Cooling minimizes lattice vibrations and thus sharpens the collected spectra. Defects in crystal structure or dopants in the material can create shallow energy states that can easily be thermalized at higher temperatures, like room temperature. Cooling reduces the ionization of these shallow energy states.

According to Saleh and Teich (1991:574), there are many mechanisms leading to absorption and emission, but the most important are: band-to-band transitions, impurity-to-band transitions, free carrier (intraband) transitions, phonon transitions, and excitonic transitions. These processes will be discussed in greater detail in Chapter 2.

1.3 Research Objectives

The purpose of this research is to determine whether or not photoluminescence can be used as a simple, non-destructive, contactless characterization method for use in the manufacturing of a particular type of InSb detector. The detectors (currently in production at L3 Communications in Mason, OH) require months to fabricate. Typically, characterization of these detectors happens at the end of the fabrication process. It is thought that if a nondestructive characterization process is implemented earlier on in the fabrication process, then defective wafers or portions of wafers can be taken out of the production line saving both time and money.

“Indium Antimonide (InSb) provides some of the highest quality, highest reliability images available in infrared imaging systems” (Davis et al. 1998:1). InSb

detectors typically operate in the 3 to 5 μm range, with a peak spectral response of about 5 μm . These detectors were originally made from single-crystal InSb, but by the late 1950's, were made out of p - n junction diodes (Dereniak & Boreman 1996:306). Advances in the fabrication of these devices continue to improve the performance of these detectors.

Today, InSb detectors are incredibly small. A single detector can have dimensions less than 100 μm in width. Many tiny detectors can be created on the same wafer, and they do not have to be completely separated. A matrix of detectors is called a focal plane array (FPA). "The format of a focal plane array is determined by the resolution and field of view (FOV) requirements of the application" (Davis et al. 1998: 1).

The 'front' side of a detector is the side containing the p n junction. Backside-illuminated detectors have the p -doped region on the under side of the detector, the side opposite incoming light. Photons enter the device and become absorbed in the n -type layer. The absorption process creates an electron-hole pair. The minority carrier is swept across the junction and collected by the circuitry. "In the case of bulk InSb material, the backside is thinned to less than the minority-carrier diffusion length" (Bloom & Nemirovsky 1991: 1792). This increases the likelihood that the carrier will be swept across the junction before recombining.

The circuitry for modern InSb photodiode detectors is a hybrid one. The InSb photodiode is created on one chip and the readout chip is created on silicon. The two chips are contacted together by indium "bumps." To ensure the indium only makes

contact where it is intended, a protective layer coats the InSb and Si surfaces where contact is not wanted. On the silicon chip, this layer is made of silicon dioxide. However on the InSb chip, another type of passivant is needed. “The issue of surface passivation is extremely important for large and dense focal plane arrays based on InSb photodiodes... The passivation must be electrically insulating as well as chemically protective” (Bloom and Nemirovsky 1993: 309). This research focuses on the effects of two types of passivation on the characteristics of the InSb substrate.

The two types of passivation in this research are a deposited layer of SiO_x and anodization. Anodization is a type of oxide grown by electrolysis. “The growth of an anodic oxide on the III-V compounds is quick and easy to accomplish. However, the process of anodization is complex and many details of the process are not well understood” (Wilmsen 1985: 430). A semiconductor sample is connected to the positive terminal of a battery and placed in an electrolyte with a cathode. For the anodization of InSb, the electrolyte is typically KOH in H_2O . In water, KOH gives up an electron, creating an OH^- ion. The ion is drawn to the semiconductor anode and reacts with the surface. The main products of the reaction are amorphous In_2O_3 and elemental Sb.

II. Theoretical Background

2.1 Chapter Overview

The purpose of this chapter is to introduce the theory behind this experiment. The chapter begins with the discussion of semiconductor basics including crystal structure and energy band structure. It continues with a discussion of various characterization methods for semiconductors. Finally, it concludes with the formulation used to analyze the data obtained from this experiment.

2.2 Semiconductor Characteristics

Crystal Structure

Solid-state materials can have their atoms arranged in a three-dimensional, repeating, periodic arrangement or can have their atoms unarranged in a chaotic manner. Materials with the periodic structure (or lattice) are called *crystalline* materials. Those without a random arrangement are called *amorphous*. Sometimes, atoms in a material can have a lattice structure when viewed microscopically, but be disordered when viewed macroscopically. These materials are *polycrystalline* materials.

The periodic structure in crystalline materials can be thought of as a unit cell repeating in space. There are many types of unit cells. One type of unit cell is simple cubic, where an atom lies at each corner of the cube (see Figure 2.1*a*). Another type is face-centered cubic (FCC). The FCC unit cell contains an atom at each corner of a cube and another atom at the center of each face of the cube (Figure 2.1*b*). A third type of unit cell is the diamond structure. It is best described as an FCC structure with another

FCC unit cell interpenetrating it, but displaced by one quarter of the diagonal, along the diagonal, of the cube (Figure 2.1c).

Certain semiconductor compounds comprised of elements from Groups III and V on the periodic table also form a structure similar to that of diamond. The diamond structure assumes all of the atoms are the same, like elemental silicon or germanium. However, for the III-V compounds, the Group-V atoms form the structure of one FCC structure and the Group-III atoms form the structure of the interpenetrating FCC lattice. The total crystal structure is called the *zincblende* structure (Figure 2.1d).

Valence Bonds

Each atom in a zincblende lattice has four closely neighboring atoms which are equidistantly spaced. If one were to draw a cube and place an atom in the center, the four nearest neighbor atoms would be located at opposite corners of each face of the cube (Figure 2.2). The length of an edge of the cube is half the size of the lattice construction but in the zincblende structure. This structure is referred to as a tetrahedron.

Each atom in the tetrahedron, and likewise the zincblende structure, shares a bond with its four nearest neighbors. This bond is mostly due to the different atoms sharing electrons, i.e., covalent bonding. In the case of the III-V compounds, “their ionic nature is quite weak, and the electrons are not strongly localized” (Ashcroft & Mermin 1976: 387).

Group-V atoms have three less electrons than a full shell. Group-III atoms have five less electrons than a full shell; this can also be thought of as having three more

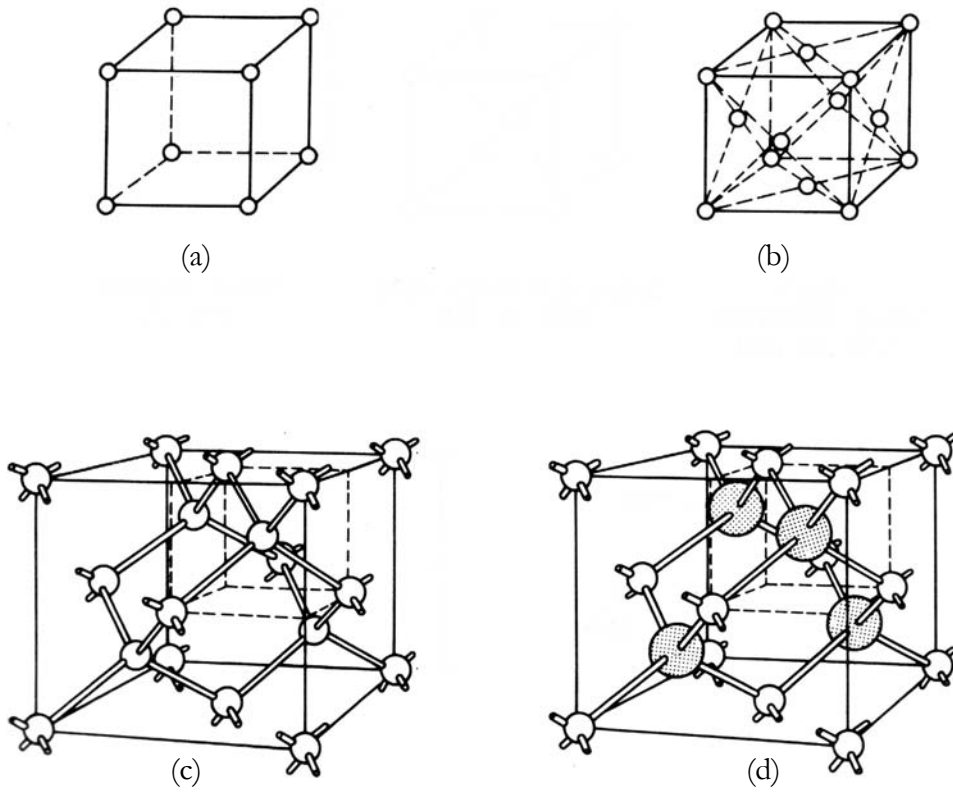


Figure 2.1. Crystalline structure unit cells. (a) simple cubic; (b) face centered cubic; (c) diamond; (d) zincblende (Sze 1981:8)

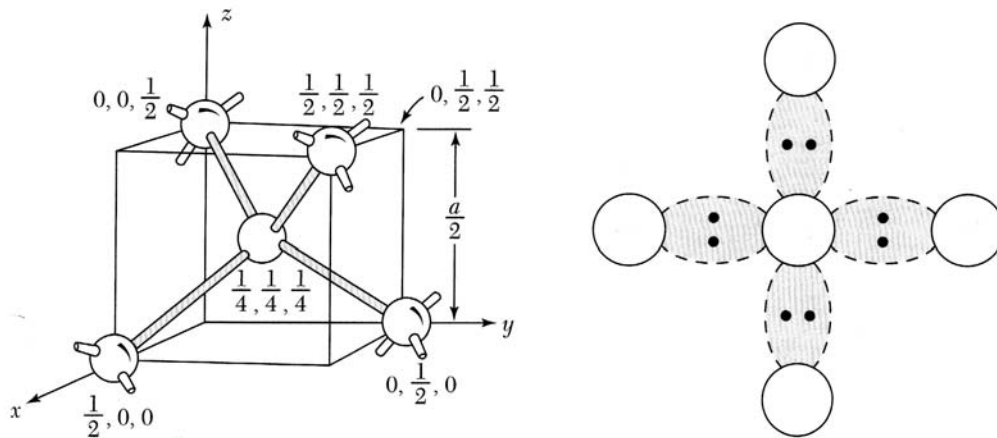


Figure 2.2. Tetrahedral Bonding (Sze 2002: 27)

electrons than a full shell. Covalent bonding occurs when atoms share electrons in order to fill their outer shell. By sharing four electrons, Groups-III and -V atoms mutually complete their outer shells, while remaining electrically neutral as a whole.

It is possible for these electrons to break their bonds and move freely throughout the lattice or crystal. This happens when additional energy is added to an electron that exceeds the bonding energy. When this occurs, the free electron can move about the lattice and conduct. The electron leaves behind a vacant location, called a *hole*. As electrons move throughout the crystal, the hole can move about, too. A hole is said to carry a positive charge and move in the opposite direction as electrons when placed under an electric field.

Energy Bands

The arrival of quantum mechanics has allowed scientists to understand the quantization of energy. For a single, one-electron atom, the energy eigenstates of the Coulomb potential are:

$$E_n = \frac{-m_e e^4}{(4\pi \epsilon_0)^2 2\hbar^2 n^2} = \frac{-13.6 \text{ eV}}{n^2}, \quad (2)$$

where n is the principle quantum number, m_e is the mass of a free electron, e is the charge of an electron, ϵ_0 is the permittivity in free-space, and \hbar is Planck's constant divided by 2π . Figure 2.3 illustrates the Coulomb potential and its eigenstates. Note that the eigenstates become more closely spaced as n increases. For positive energies, i.e., unbound electrons, the electrons can exist in an effective continuum of eigenstates.

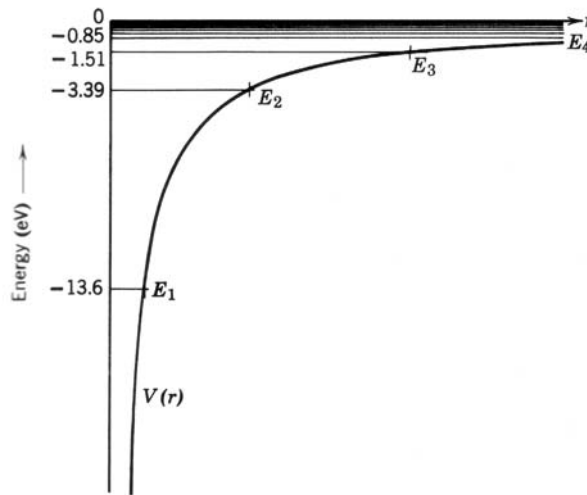


Figure 2.3. Coulomb potential and its eigenstates (Eisberg & Resnick 1985:239)

Now consider two one-electron atoms that are spaced infinitely apart. The energy eigenstates for each atom are the same. However, when these atoms are brought closer together, the Pauli Exclusion Principle causes these states to split. For each level of E_1 , E_2 , etc., there are now two levels at each energy state (see Figure 2.4.) Similarly, for four identical atoms, each level splits into four levels. As the number of atoms increases, the closely spaced eigenvalues form a continuum of energy states, or an energy band, for each principle quantum number.

In the case of semiconductors, the inner electrons contained in closed shells are tightly bound by the nucleus. These electrons occupy the lowest energy level in Figure 2.4. The outer electrons, called the valence electrons, are located farther from the nucleus and do not have the strong bond that the inner electrons have. These are the electrons that have the greatest probability to interact with other electrons of other atoms and can participate in conduction.

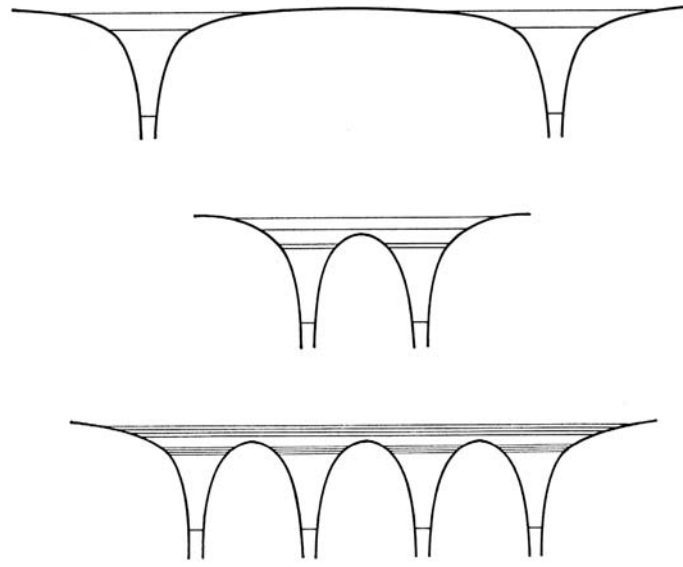


Figure 2.4. Eigenstate splitting due to interactions with nearby atoms (Eisberg & Resnick 1985:447)

The energy of an electron is also determined by other quantum numbers including the angular momentum quantum number. The angular momentum quantum number corresponds to the sub-shells commonly called s , p , d , and f . The s sub-shell can contain up to two electrons. The p sub-shell can contain up to six electrons. Taking this into consideration, the spacing between eigenstates becomes almost continuous as atoms are brought closer together. Figure 2.5 shows the formation of energy bands as carbon atoms are brought closer together in the formation of a diamond lattice.

At absolute zero temperature, electrons fill up the lowest energy states available. These states are called the valence states, and in the case of the semiconductor crystal, they are valence bands. Eigenstates of higher energies are conduction states and the continuum of energy states is called the conduction band. The spacing between the top of the valence band and the bottom of the conduction band is the bandgap. This

corresponds to the energy required for an electron to break its bond and move throughout the crystal.

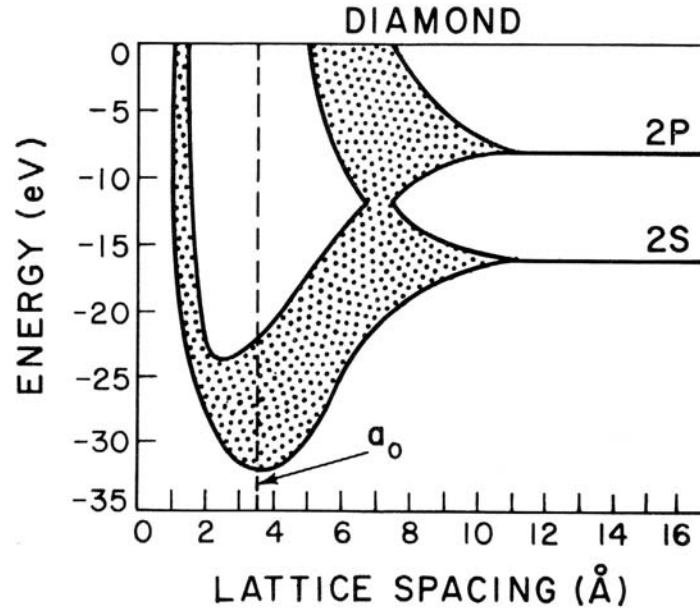


Figure 2.5. Energy band formation as atoms are brought closer together in a diamond lattice structure (Willardson & Beer 1967:197)

The energy of an electron can also be described in terms of momentum. In terms of a free electron, the energy is described as:

$$E = \frac{p^2}{2m_0}. \quad (3)$$

where p is the momentum and m_0 is the mass of a free electron.

As the absolute value of the momentum increases, the energy increases parabolically. Electrons in semiconductors are not entirely free, even when in the conduction states. Therefore, an effective mass is used in Equation (3). Effective mass is a property of the semiconductor. Different effective masses are used for electrons in

the conduction band and holes in the valence band. The effective mass of a hole is typically larger than that of an electron, causing the shape of the valence band parabola to be wider than that of the conduction band. Sometimes, it is necessary to discuss the reduced mass of a system. Reduced mass comes from the effective electron and hole masses, i.e.,

$$m_r = \frac{m_e m_v}{m_e + m_v}, \quad (4)$$

where m_e is effective electron mass and m_v is the effective hole mass.

A hole in the valence band is thought of as a vacant state in the conduction band being excited into the valence band just as an electron is excited from the valence band into the conduction band. Typically, the top of the valence band is considered to be zero energy and increasing hole energy is negative. Therefore, energy band diagrams often have one inverted parabola whose maximum is at zero energy and another parabola whose minimum is E_g (the value of the energy gap) above zero energy as shown in Figure 2.6.

Crystal orientation also plays a key role in value of the effective mass, and hence, the shape of the bands as a function of momentum. Recall in Figure 2.2 that each In atom in the zincblende crystal structure is tetrahedrally bonded to four Sb atoms. “The occupation of adjacent sites by different atoms in the zincblende lattice results in an absence of the inversion symmetry which is present in the diamond lattice. This difference between the two closely related crystal types leads to certain small

fundamental differences between the energy band structures of elemental...” (Long 1968:15).

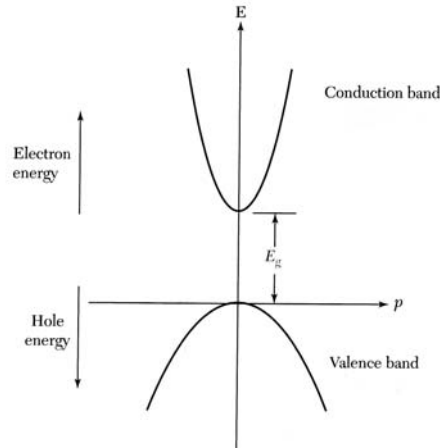


Figure 2.6. Parabolic energy band diagram. (Sze 2002:3)

InSb is a *direct-gap* semiconductor because the valence band maximum and conduction band minimum occur at the same momentum. In some crystals, the conduction band minimum and valence band maxima occur at different momenta. This requires an electron to not only gain E_g in energy, but to change its momentum, as well. These crystals are called *indirect* gap semiconductors. However, for InSb, “only in the extremes of high temperature or high free-electron concentration do multivalley effects become evident” (Rode 1971: 3287).

Carriers in Thermal Equilibrium

Thermal equilibrium is a steady-state condition in which there are no external excitations of electrons. Temperature is considered constant, but the system is not necessarily at zero Kelvin. At temperatures greater than zero Kelvin, an electron can be

thermally excited into the conduction band and, thus, can create a hole in the valence band.

The number of electrons in the conduction band at a given temperature is based upon the product of the number of states per energy per unit volume that are available into which the electron may be excited, and the probability that an electron will be excited into that state. The probability is given by Fermi-Dirac statistics (Huang 1987: 245). The Fermi distribution function is:

$$f(E) = \frac{1}{e^{(E-E_f)/k_B T} + 1}, \quad (5)$$

where E_f is the Fermi energy, k_B is Boltzmann's Constant, and T is the absolute temperature. The Fermi energy is the energy at which the probability is 50%. The density of states is given by two separate functions. For the conduction band,

$$g_c(E) = \frac{(2m_c)^{\frac{3}{2}}}{2\pi^2\hbar^3} (E - E_c)^{\frac{1}{2}}, \quad (6)$$

where m_c is the effective mass of an electron and E_c is the conduction band minimum energy. Similarly, for the valence band,

$$g_v(E) = \frac{(2m_v)^{\frac{3}{2}}}{2\pi^2\hbar^3} (E_v - E)^{\frac{1}{2}}. \quad (7)$$

where m_v is the effective mass of a hole and E_v is the valence band maximum energy.

Thus, the thermal-equilibrium electron carrier concentration is:

$$n_0 = \int_{E_c}^{\infty} g_c(E) f(E) dE . \quad (8)$$

Substituting the Fermi distribution function and electron density of states yields,

$$n_0 = \frac{(2m_c)^{\frac{3}{2}}}{2\pi^2 \hbar^3} \int_{E_c}^{\infty} \frac{(E - E_c)^{\frac{1}{2}}}{1 + e^{\frac{(E - E_f)}{k_B T}}} dE, \quad (9)$$

Conversely, the thermal-equilibrium hole concentration is:

$$p_0 = \int_{-\infty}^{E_v} g_v(E) [1 - f(E)] dE , \quad (10)$$

which upon substitution yields,

$$p_0 = \frac{(2m_v)^{\frac{3}{2}}}{2\pi^2 \hbar^3} \int_{-\infty}^{E_v} \frac{(E_v - E)^{\frac{1}{2}}}{1 + e^{\frac{(E_f - E)}{k_B T}}} dE. \quad (11)$$

Note the probability in the hole concentration is based on the probability that an electron is *not* occupying a state in the conduction band. Figure 2.7 shows examples of the density of states, Fermi distribution function, and carrier concentrations.

The carrier concentration of a semiconductor can also be altered using intended impurities. These intended impurities are called dopants. A doped semiconductor is considered to be extrinsic, whereas an undoped sample is called intrinsic. Dopants are atoms that take the place of the normal elements in the crystal structure and either a) add extra electrons, causing the system to have an excess of negative carriers, or b) add an extra hole to the system, causing the material to have an excess positive charge.

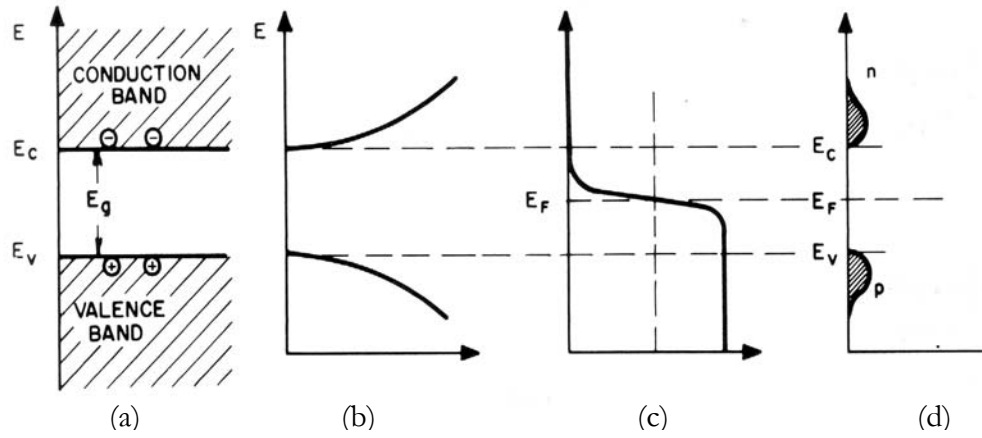


Figure 2.7. (a) flat energy band diagram and (b) corresponding density of states, (c) Fermi distribution function, and (d) carrier concentrations. (Sze 1981: 23)

Dopants that add electrons to the system are said to donate an electron and are thus called donor atoms. Donor ions occupy an energy state below the conduction band. Typically, donor ionization energies lie within a few percent of the bandgap from the conduction band edge; however, there do exist lower lying ionization states often referred to as low-level or deep-donor states.

Dopants that add holes to the system are said to accept electrons and are thus called acceptors. Similarly, acceptor ions occupy an energy state above the valence band. Although the dopants add carriers to the system, the law of mass action requires that the product of electron and hole carrier concentrations is equivalent to the intrinsic electron concentration squared, i.e.,

$$n_0 p_0 = n_i^2, \quad (12)$$

where n_i is the intrinsic carrier concentration.

Injection and Quasi-Fermi States

When a semiconductor is being injected with carriers from a current or by bombardment of photons, the semiconductor is no longer in thermal equilibrium. In the case of photon bombardment, the photon flux induces band-to-band transitions so quickly that interband equilibrium cannot be achieved. However, intraband equilibrium is still possible. That is, there are “situations in which the conduction-band electrons are in thermal equilibrium among themselves, as are the valence-band holes, but the electrons and holes are not in mutual thermal equilibrium” (Saleh & Teich 1991:558). Therefore, the carrier distribution for semiconductors injected with carriers is best described by two separate Fermi functions, one for each bands.

Once pumping commences, the generation of electron-hole pairs in addition to the thermal generation of pairs will be at a rate,

$$R = \frac{\Delta n}{\tau}, \quad (13)$$

where Δn is the concentration of generated electron-hole pairs, and τ is electron-hole recombination lifetime. The concentration of generated electron-hole pairs can also be determined from the pump laser. The product, $R\tau$, is related to the wavelength or energy of the laser used for pumping, the pump power, and the volume of material being optically pumped. The generated electron-hole pair concentration is then described as

$$\Delta n = \frac{\Phi_{pump} \cdot \eta}{E_{photon} \cdot V}, \quad (14)$$

where Φ_{pump} is the optical pump power, η is the quantum efficiency, E_{photon} is the photon energy, and V is the volume of material being optically pumped.

Increasing the pump power increases the generated carrier concentration.

This generation of electron-hole pairs results in a total carrier concentration value of

$$n = n_0 + \Delta n \quad (15)$$

for electrons, and similarly for holes,

$$p = p_0 + \Delta p. \quad (16)$$

The generated carrier densities give insight as to what the levels of the separate Fermi energies are. Similar to Equation (8), the quasi-thermal-equilibrium electron concentration is:

$$n_0 + \Delta n = \frac{1}{2\pi^2} \left(\frac{2m_c}{\hbar} \right)^{\frac{3}{2}} \int_{E_c}^{\infty} \frac{(E - E_c)^{\frac{1}{2}}}{1 + e^{(E - E_{fc})/k_B T}} dE, \quad (17)$$

where E_{fc} is quasi-Fermi energy in the conduction band, and similar to Equation (11), the quasi-thermal-equilibrium hole concentration is:

$$p_0 + \Delta p = \frac{1}{2\pi^2} \left(\frac{2m_v}{\hbar} \right)^{\frac{3}{2}} \int_{-\infty}^{E_v} \frac{(E_v - E)^{\frac{1}{2}}}{1 + e^{(E_{fv} - E)/k_B T}} dE, \quad (18)$$

where E_{fv} is quasi-Fermi energy in the valence band.

From the quasi-Fermi energies, it is possible to obtain the quasi-Fermi distributions for the conduction and valence bands. For the conduction band,

$$f_c = \frac{1}{1 + e^{(E_2 - E_{fc})/k_B T}}, \quad (19)$$

where E_2 is an energy within the conduction band. Similarly, for the valence band,

$$f_v = \frac{1}{1 + e^{(E_1 - E_{fv})/k_B T}}, \quad (20)$$

where E_1 is an energy within the valence band.

2.3 Absorption and Emission of Photons

Absorption occurs when an electron gains enough energy from an incident photon to transition from a lower to higher energy state. Emission occurs when an excited electron gives off energy, dropping it into a lower energy state. The act of an electron dropping from a conduction band state into a valence band state is the same as the recombination of an electron and hole, since the definition of a hole is the absence of an electron. For emission of a photon, the energy of the photon must be equal to the difference in energies of the electron and hole, or the conduction band state and the valence band state. For direct-gap semiconductors, like InSb, this is solely a transition in energy, not a transition in momentum.

In addition to the conservation of energy, another condition of absorption is that there exists a higher energy state for the electron to be excited into. On the other hand, for emission to occur, there needs to exist a lower energy state for the electron to fall

into. The density of states in the conduction and valence bands were defined in Equation (6) and (7), respectively. For absorption and emission, these can be combined into what is referred to as the *optical joint* density of states,

$$g(h\nu) = \frac{(2m_r)^{\frac{3}{2}}}{\pi\hbar^2} (h\nu - E_g)^{\frac{1}{2}}, \quad (21)$$

for energies greater than the bandgap energy.

Similarly, the Fermi distribution has an optical form for emission or absorption. For emission, this is a product of the probabilities that an electron occupies a conduction state, E_2 , and a hole occupies a valence state, E_1 . Therefore, the Fermi distribution for emission is:

$$f_e(h\nu_{21}) = f_c(E_2)[1 - f_v(E_1)]. \quad (22)$$

Conversely, the Fermi distribution for absorption is:

$$f_a(h\nu_{12}) = [1 - f_c(E_2)]f_v(E_1). \quad (23)$$

Provided that the quasi-Fermi levels are sufficiently far from the energy states E_1 and E_2 ,

$$f(E_2) \approx e^{-(E_2 - E_{fc})/k_B T}, \quad (24)$$

and

$$[1 - f(E_1)] \approx e^{-(E_{fv} - E_1)/k_B T}. \quad (25)$$

The spectral intensity for emission then becomes the proportional to the product of the optical joint density of states and the probability of emission, i.e.,

$$I(h\nu_{21}) = \frac{1}{\tau_r} g(h\nu_{21}) f_e(h\nu_{21}). \quad (26)$$

Equation (26) is valid for energies greater than or equal to the bandgap energy.

Absorption Fundamentals

Absorption measurements often impart a broad spectrum of energy or wavelengths onto a sample. This allows the researcher to gain knowledge of the energy levels of in a material (Pankove, 1971:34). Absorption techniques are based upon transmission measurements. A variable wavelength light source falls incident upon a sample. A fraction of that light is absorbed in the material. Another fraction is reflected. A third fraction is transmitted through the material. The sum of these fractions will equal the total intensity of the incident beam. Mathematically, this can be written as,

$$I_0 = I_a + I_r + I_t, \quad (27)$$

where I_0 is the intensity of light source incident on the sample, I_a is the intensity of light absorbed in the sample, I_r is the intensity of light reflected off the sample, and I_t is intensity of light transmitted through the sample. Dividing both sides of Equation (27) by the light incident on the sample yields,

$$1 = \frac{I_a}{I_0} + \frac{I_r}{I_0} + \frac{I_t}{I_0} = \mathbf{A} + \mathbf{R} + \mathbf{T}, \quad (28)$$

where A is the absorptance, R is the reflectance, and T is the transmittance. Therefore, absorptance, transmittance, and reflectance are fractions of the incident beam.

When taking actual measurements, it is often easier to measure transmittance. Typically, a source shines normally upon a sample and a photodetector measures the transmitted light. This transmitted spectrum is then compared to the spectrum without the sample in place, known as the background measurement. The ratio of the sample spectrum to the background spectrum is equivalent to the transmittance,

$$T_{measured} = \frac{I_t}{I_0} = \frac{I_{sample}}{I_{background}}, \quad (29)$$

where $T_{measured}$ is the measured transmittance, I_{sample} is the intensity of the light source transmitted through the sample, and $I_{background}$ is intensity of light incident on the sample.

In some fields, *absorbance* is used instead of absorptance. Absorbance is based on measured transmittance, however, it is not a percentage of the absorbed light.

Absorbance is the logarithm with base 10 of the inverse measured transmission, i.e.,

$$Abs = \log_{10} \left(\frac{1}{T_{measured}} \right) = \log_{10} \left(\frac{I_{background}}{I_{sample}} \right). \quad (30)$$

From the transmitted intensity and incident intensity, the absorption coefficient of the material can be determined. “The absorption coefficient, $\alpha(\hbar\omega)$, is related to the relative decrease of light intensity, \mathcal{I} , as it passes through the absorption medium, according to

$$\alpha = -\frac{1}{\mathcal{I}} = \frac{d\mathcal{I}}{dx}, \quad (31)$$

or

$$-\frac{d\mathcal{I}(x)}{dx} = \alpha\mathcal{I}(x). \quad (32)$$

The solution to this equation is

$$\mathcal{I}(x) = \mathcal{I}_i e^{-\alpha x}, \quad (33)$$

where \mathcal{I}_i is the intensity of the incident light. If the sample thickness is d , then the intensity of the transmitted light falling on the detector is

$$\mathcal{I}_d = \mathcal{I}_i e^{-\alpha d}. \quad (34)$$

In terms of the measured quantities, the absorption coefficient becomes

$$\alpha = -\frac{1}{d} \ln \left(\frac{I_{sample}}{I_{background}} \right). \quad (35)$$

The value of α will depend on photon energy or wavelength” (Bhattacharya 1993:149).

The relationship of absorption coefficient to energy is:

$$\alpha(h\nu_{12}) = \frac{\sqrt{2}m_r^{\frac{3}{2}}c^2}{\tau_r(h\nu_{12})^2} (h\nu_{12} - E_g)^{1/2} [f(E_1) - f(E_2)]. \quad (36)$$

The majority of radiative absorption occurs in band-to-band transitions. However, there are other transitions which can occur. Acceptor and donor impurity states allow for transitions between the impurity state and conduction or valence band. An electron in the valence band can absorb enough energy to be excited into an acceptor state, a donor state, or directly to the conduction band. An electron in an acceptor state can be excited into either a donor state or conduction band. An electron in a donor state can be excited into the conduction band. These transitions are shown in Figure 2.8.

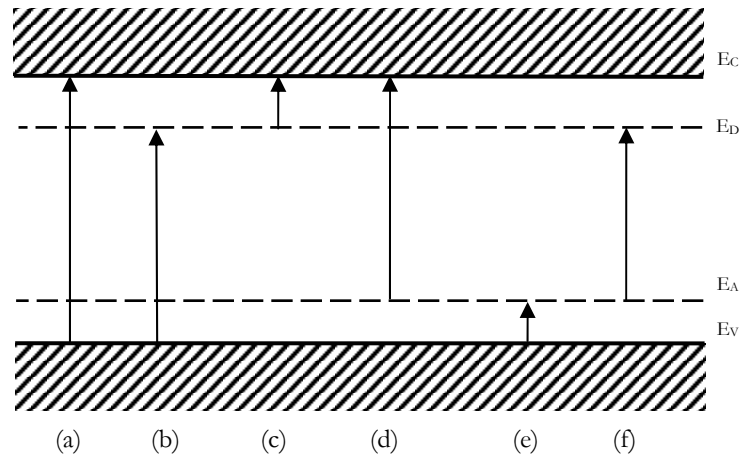


Figure 2.8. Absorptive transistions. (a) band to band; (b) valence band to donor state; (c) donor to conduction band; (d) acceptor to conduction band; (e) valence band to acceptor level; (f) acceptor level to donor level

Another cause for absorption is due to excitons. Excitons are electron-hole pairs that orbit each other instead of annihilate themselves. They are attracted by their opposite charge, much like a hydrogen atom. This Coulomb attraction allows the excitons to move freely about a material as a pair. The binding energy of an exciton is very small, on the order of 0.43 meV for InSb (Haug & Koch 2004: 176). This binding

energy is equivalent to $k_B T$ at 4.99 K. Therefore, the exciton energy state is slightly below the conduction band but is usually thermalized above 5 K.

Photoluminescence Fundamentals

Photoluminescence measurements allow one to gain knowledge from emission of photons from a material. Photoluminescence experiments consist of a single wavelength energy beam (typically a laser) that is of high enough energy to excite electrons from the conduction band into the valence band. This creates electron-hole pairs that, when recombined, give off energy in some form. Radiative recombination occurs when the energy given off as an electron-hole pair recombines is in the form of a photon.

The photon emission observed at different material temperatures and various laser excitation powers yields insight to the energy bands of a semiconductor. As discussed in Section 2.3, the spectral intensity for emission is proportional to the optical joint density of states and the quasi-Fermi levels. Increasing the pump power increases the energy of the quasi-Fermi level which, for band-to-band transitions, increases the width of the emission spectral intensity. Temperature changes alter both the Fermi distribution and the density of states. Therefore, by investigating the effects of temperature and optical pump power, one can gain knowledge about the energy bands and the probabilities for photon emission.

2.4 Relevant Research

Much work has been done on InSb. In fact, there seems to be some disagreement with reported material properties amongst scientists. Below is a chart of

the differences between material parameters as recorded in various textbooks and articles.

Table 1. Comparison of InSb material properties

Source	$E_g(0\text{ K}) \{ \text{eV} \}$	$\mu_c(300\text{ K}) \{ \text{cm}^2/\text{Vs} \}$	$\mu_v(300\text{ K}) \{ \text{cm}^2/\text{Vs} \}$	$n_i(300\text{ K}) \{ \text{cm}^{-3} \}$
Ashcroft & Mermin 1976: 566, 570	0.23	$0.015\ m_0$	$0.015\ m_0$	---
Dereniak & Boreman 1996: 306	0.233	---	---	---
Madelung 2004: 154-158	0.23632	$0.0118\ m_0$	$0.016\ m_0$	1.89×10^{16}
Moss 1959: 226-257	0.26	$0.013\ m_0$	$0.018\ m_0$	1.6×10^{16}
Rogalski et al. 2000: 18	0.2357	$0.0116\ m_0$	$0.0149\ m_0$	1.9×10^{16}

Much of the disagreement in Table 1 lies in how the researchers obtained the values for bandgap energies from their absorption data. For example, Moss (1959:40) defines “the ‘absorption edge’ as the point where the slope of the absorption coefficient is a maximum.” This definition gives higher values of bandgap energy. On the contrary, Saleh & Teich (1991:586) use the optical joint density of states minimum energy to define the absorption edge or bandgap of the material. Another cause for disagreement is the quality of the material. “Development of [InSb] crystal growth techniques in the early fifties...has improved immensely” (Rogalski et al. 2000:16). Modern techniques for single crystal growth of InSb have greatly reduced the amount of impurities in the samples.

For this research, Logothetidis & Cardona (1985: 947) as reported in Madelung (2004: 155) was used as the standard for determining theoretical bandgap energies as a function of temperature. The temperature dependence of the energy gap was modeled using the Varshni equation and defined as:

$$E_g(T) = E_g(0\text{K}) + \frac{\alpha_v T^2}{(\beta_v + T)}, \quad (37)$$

where α_v is 0.6 meV/K and β_v is 500 K. A plot of InSb bandgap temperature dependence as defined by Equation (37) is shown in Figure 2.9.

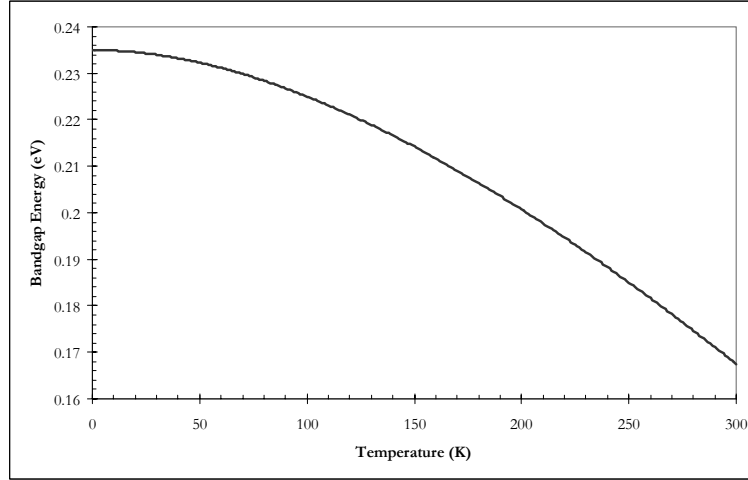


Figure 2.9. Temperature dependence of bandgap energy for InSb as defined in Equation (37)

Rowell (1988:37) reported on photoluminescence of (100) InSb. He used a Fourier-Transform spectrometer to collect the emission. The optical pump beam came from an argon ion laser (2.410 eV) with a 1 mm beam diameter. Samples were cooled using a Janis Supertran cryostat. Sample temperature was varied from 5 to 20 K and pump power was varied from 15 to 200 mW (see Figure 2.10).

Rowell observed three peaks in the photoluminescence spectra. One peak was labeled as band-to-band transitions. The intensity and full-width-half-max (FWHM) both increased with increased laser pump power. The integrated intensity increased quadratically. Peak energy at 5.1 K was 0.23443 eV, and 0.23436 eV at 18.1 K.

A second, much smaller peak was observed at slightly lower energy. Its intensity only increased slightly with laser power, but decreased rapidly with temperatures above 10 K. This was labeled as the bound-exciton peak.

The third peak observed by Rowell was classified as an impurity peak. It had an intensity that increased linearly with pump power and also increased with temperature. This transition occurred about 6.3 meV below the band-to-band emission line and was determined to be a Group-II element, possibly Zn or Cd.

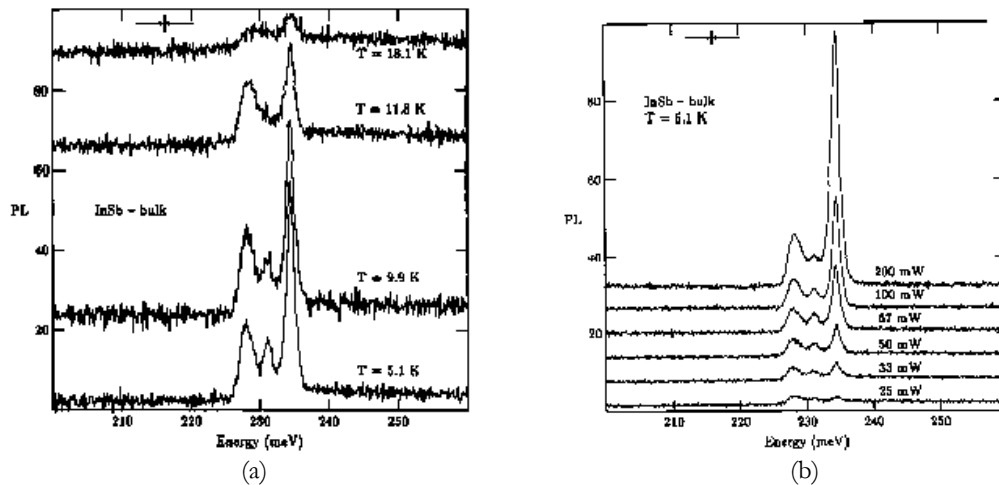


Figure 2.10. Rowell's (1988:40) photoluminescence spectra. (a) photoluminescence spectra of InSb with varying temperatures and 67 mW pump power. (b) photoluminescence spectra of InSb with varying pump power at 5.1 K.

In the 1990's, Bloom and Nemirovsky published a number of papers on backside-illuminated InSb detectors. Their focus was not on InSb characterization, but on device design. In their February 1993 article, they discuss surface passivation of etch-thinned InSb wafers. They passivated their samples by depositing SiO_x on both front and back surfaces. They found that the surface passivation on the doped side of an InSb diode determines the behavior of reverse-bias characteristics but “the electrical

performance of photodiodes ...is limited by the properties of the starting bulk material” (Bloom & Nemirovsky 1993: 313).

Mattausch and Aspnes, however, looked at the optical properties of anodized InSb in their February 1981 journal. Their research focused on the 1.5- to 6-eV spectrum, much higher energies than that of the InSb bandgap. They found the absorption edge of the anodic oxide (In_2O_3) to be 3.8 eV with an absorption tail stretching to at least 1.5 eV. They correlate this long absorption tail to a characteristic of amorphous materials. They also found Sb_2O_3 to have a threshold energy of 4.4 eV. These energies are far above the bandgap of InSb meaning that the anodization layer should be transmissive of lower energy light.

2.5 Summary

InSb, a III-V semiconductor, crystallizes in the zincblende structure. The act of bringing those atoms together in a crystal structure creates energy bands and energy gaps. The number of possible energy states at a certain energy level is given by the density of states. Fermi-Dirac statistics determine the probability that an electron is in a particular energy state. Optically exciting an InSb sample creates quasi-Fermi energy levels, which, by increasing the concentration of recombining carriers per unit volume, will cause photon emission to increase in energy density.

Absorption is determined by imparting a broad-spectrum source onto a sample and measuring the transmitted and incident light. Knowing the thickness of a sample allows one to determine the absorption coefficient, which is related to the density of states and Fermi levels. From the density of states, one can determine the energy gap.

Photoluminescence measurements include a narrow band, higher powered source. Light from this source falls incident upon a sample and is absorbed. As electrons and holes are created by absorption, they also recombine, giving off photons. The spectral density of these photons is dependent upon the power per unit volume of the source and provides information on the transitions occurring in the sample.

Rowell (1988) showed that band-to-band, impurity, and bound-exciton emissions can be observed using an FT-IR spectrometer by optically exciting InSb samples. Bloom and Nemirovsky (1993) showed that SiO_x does not effect the electronic characteristics of the bulk InSb. Mattausch and Aspnes (1981) demonstrated that the absorption threshold of anodic oxide should be above the bulk InSb absorption edge. All these are pertinent to the research done here.

III. Experimental Methods

3.1 Chapter Overview

The purpose of this chapter is to discuss the equipment and methods of data collection. It serves as a guide for those wishing to repeat or later build upon this experiment. Model numbers and vendors are included in the discussion. The chapter begins with preparation of the samples. It continues with information on the cryogenic system used for the experiment and concludes with the absorbance and photoluminescence spectroscopy.

3.2 Sample Preparation

Three half-wafers were obtained from L3 Communications in Mason, OH. The wafers consist of a 3-inch diameter InSb substrate. The angle between the primary and secondary flats is 90° . This implies the wafers are oriented in the $\langle 100 \rangle$ direction per Semiconductor Equipment and Materials International (SEMI) standard (Jaeger 2002:20). One wafer has a 700-Å layer of silicon oxide (SiO_x). The second wafer has been anodized. The third wafer is bare and has no extra layers added to it (see figure 3.1). Samples were cleaved along the flat edge of each half-wafer; each sample measured 1 cm x 1 cm square.



Figure 3.1. Cross view of wafers and their layers.

3.3 Cryogenic System

Samples are cooled using a Helitran® Open Cycle cryogenic refrigeration system, model LT-3-110, obtained from Advanced Research Systems, Inc. (see Figure 3.2). The system uses liquid helium (or nitrogen) to cool the sample via conduction. It allows users to perform experiments at temperatures ranging from about 4.2 to 300 K.

Each sample is attached to the sample holder using a very small dab of rubber cement. The rubber cement physically and thermally bonds the sample to the copper plate of the sample holder. Rubber cement is ideal as a type of bonding material due to its high thermal conductivity at low temperatures and its ability to be easily removed from a sample without damage (O'Brian & Witteborn 1984).

For absorption measurements, the sample is centered over a 5-mm diameter opening on a copper plate in the sample holder. For photoluminescence measurements, the samples are placed on a solid copper plate. A radiation shield is installed that surrounds the sample holder and limits the radiant heat load on the sample holder and cold stage. A vacuum shroud then seals the chamber from the exterior. There are two radiation shields designed differently for absorption or photoluminescence experiments. The one for absorption is designed to allow light to pass directly through the chamber, whereas the one for photoluminescence is designed to allow light to enter and exit at a range of angles with a maximum angle of 180° .

The vacuum shroud has removable plates on all four sides of the chamber where the sample holder is located. Two of the plates were removed and replaced with

mounted zinc selenide (ZnSe) windows. Transmission of ZnSe ranges from 0.6 to 20 μm (see Figure 3.3). For absorption measurements, these windows are placed across from each other allowing light to pass directly through the cryostat. For photoluminescence, the windows are placed on adjacent sides, allowing laser light to enter the chamber and photoluminescence to exit the adjacent side.

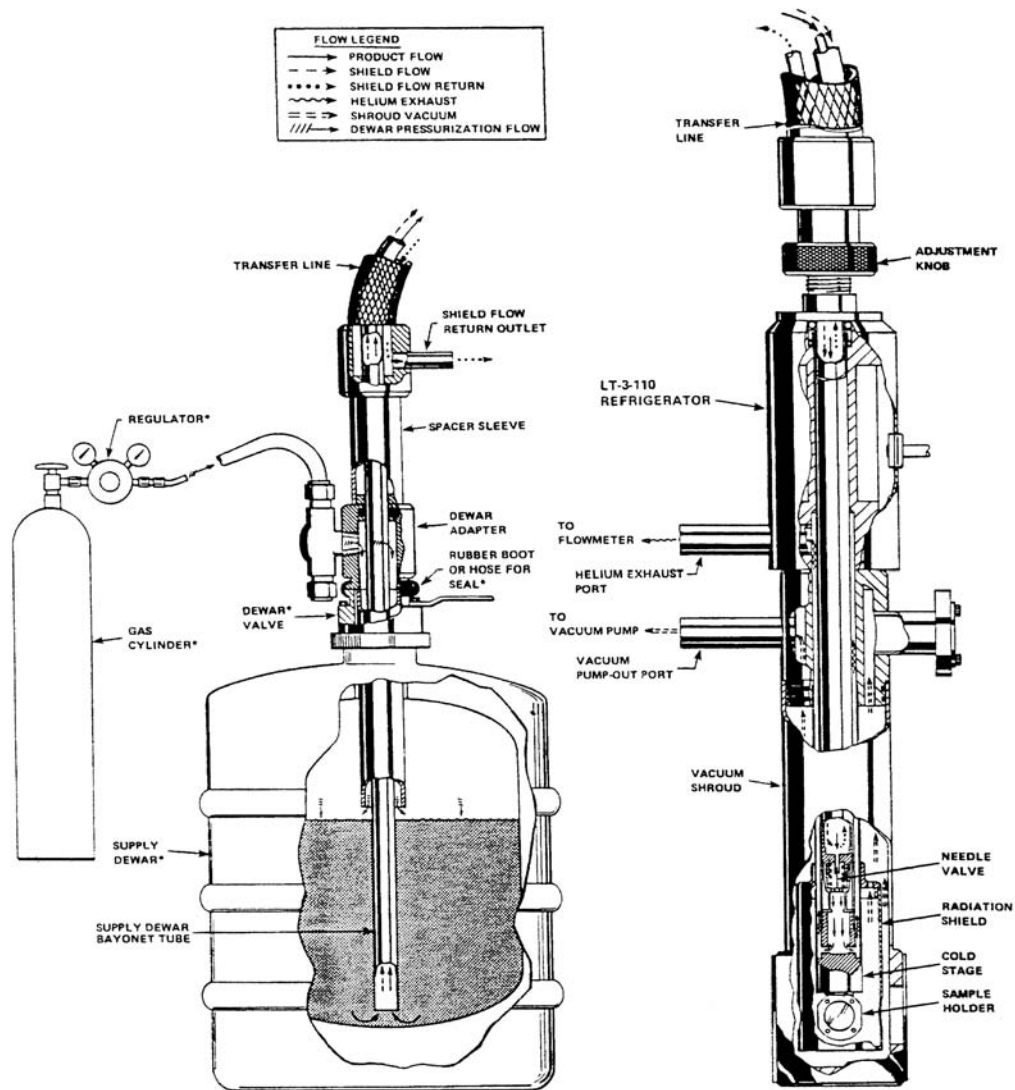


Figure 3.2. Helitran open cycle cryogenic refrigeration system. (ARS 2001)

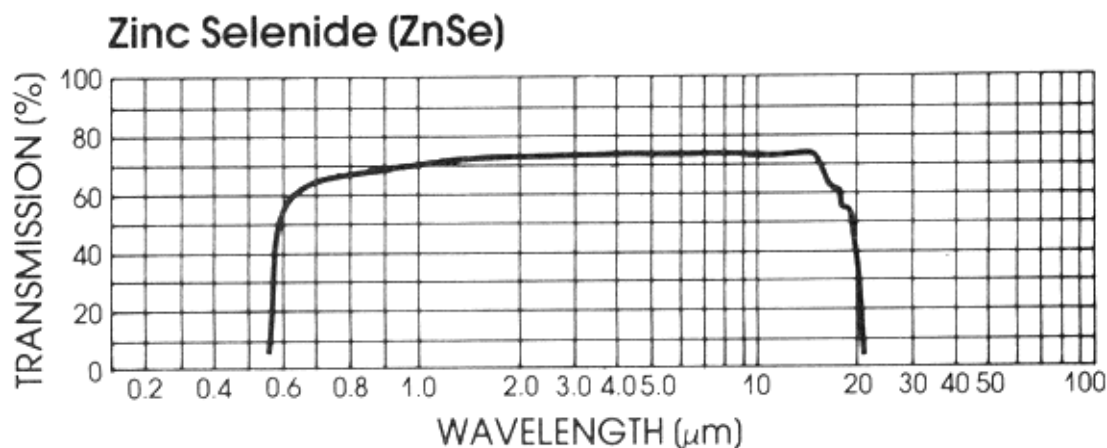


Figure 3.3. Transmission spectrum of zinc selenide windows (Del Mar Ventures 2006)

A mechanical pump is used to evacuate gases including water vapor inside the chamber. Once the chamber has reached an interior pressure of at most 0.05 Torr, the cryostat can be cooled. This vacuum step is critical as sweating and frosting can occur if vapors are still in the chamber when it begins to cool. These vapors also exchange heat via convection and will not allow the chamber to cool correctly.

Cryogenic liquid is transferred from a pressurized dewar into the refrigerator. A needle valve located near the tip of the cold finger regulates liquid flow to the cold stage via an external dial. Liquid passing through the valve cools the cold stage to which the sample holder is attached. Helium (or nitrogen) exhaust is used to pre-cool the supply line before exiting the system.

The temperature of the sample holder is controlled via an external temperature controller. This system uses Model 331S Temperature Controller from Lake Shore Cryogenics, Inc. It consists of two temperature sensors, a heater, and a control box. The heater and one temperature sensor are located on the tip of the cold finger. The other temperature sensor is located on the sample holder near the sample. When a

desired temperature is set on the control box, the temperature controller then uses algorithms to vary the current in the heater to reach and stabilize at the set temperature. Either of the two sensors can be used to control the temperature.

3.4 FT-IR Spectroscopy

Absorption

Absorption measurements were performed using an FT-IR system. The FT-IR spectrometer is based on a Michelson interferometer (see Figure 3.4). An infrared source of radiation falls incident on a beamsplitter. A fraction of the beam is reflected and sent towards a fixed mirror. The beam is then reflected off the fixed mirror, sent back through the beamsplitter, through the sample and finally reaches the detector. The remaining fraction of source beam travels through the beamsplitter to a movable mirror and is reflected back to the beamsplitter. Upon reaching the beamsplitter, the light is reflected towards the detector.

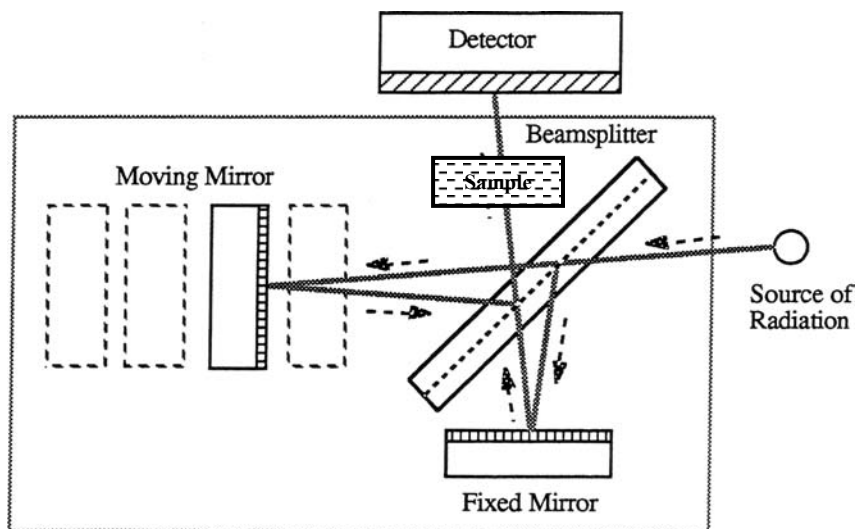


Figure 3.4. Michaelson Interferometer. The beams are displaced for clarity. (Adapted from Bio-Rad Laboratories 1992)

The two beams recombine at the beamsplitter and travel through the sample and then to the detector. When the path length to the movable mirror and the fixed mirror is identical, the beams interfere constructively. However, when the movable mirror changes location, the two beams will be out of phase. The movable mirror translates slowly over a set time interval, and as it moves, the detector records the summation of constructive and destructive interference of the beams as an interferogram. The interferogram is then Fourier-transformed, resulting in a spectrum of detector response versus wavenumber.

The FT-IR system used in this experiment is the Bio-Rad model FTS-60A obtained from Varian. The FTS-60A spectrometer can be set up to have a series of different optical sources, detectors, and beamsplitters. In this experiment, the 3- to 8- μm range was of particular interest. Therefore, the globar source and the deuterated triglycine sulfate (DTGS) detector were chosen. This pair required use of the potassium bromide (KBr) beamsplitter.

The Bio-Rad FT-IR spectrometer can be set to several parameters. Resolution can be set from 0.25 to 32 cm^{-1} . In this experiment, resolution was set to 1 cm^{-1} . Resolution corresponds to the incremental steps in wavenumber to record. A resolution of 1 cm^{-1} is equivalent to a 0.964406 wavenumber increment.

The system can average out several scans to help increase the signal-to-noise ratio. Noise is “a random fluctuation in instantaneous value of a parameter” (Hengehold 2004: OD I-6). Therefore, averaging out the random fluctuations yields a more precise result. The ‘scans to co-add’ parameter of the Bio-Rad FT-IR determines how many

scans will be used to average the result. Figure 3.5 compares the fluctuations at room temperature with no signal for a single scan, 100 scans, and 200 scans. The root-mean-square of the spectral response for the single scan, 100 scans, and 200 scans was 2.68×10^{-3} , 1.35×10^{-3} , and 1.35×10^{-3} , respectfully. Therefore, the signal-to-noise ratio of the single scan is half of the signal-to-noise ratio for 100 or 200 scans. The 100 scans measurement took 6 minutes to execute. The 200 scans took 11 minutes to complete. Therefore, it was determined that the 100 scans would be sufficient.

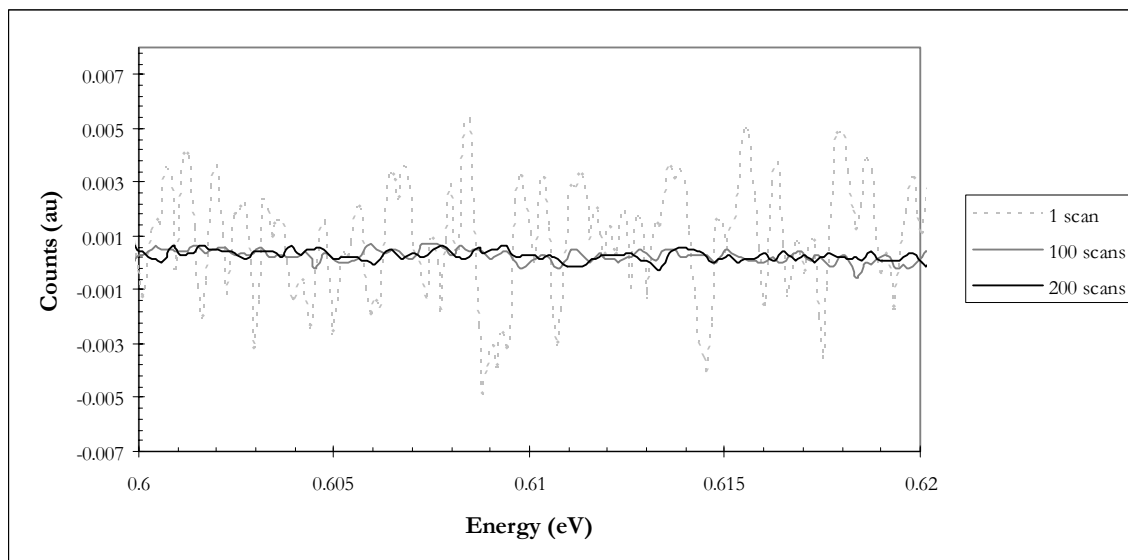


Figure 3.5. Noise test of Bio-Rad scans to co-add.

A measurement of the ‘background’ is taken first. It is used to determine the effects of anything other than the sample. It is like a measurement of the incident radiation. The cryostat (or other sample holder) is placed in the FT-IR spectrometer. A spectrum is collected with the same parameters as with the samples.

When a background has been taken, a sample is placed in the cryostat. The sample is then cooled using liquid helium. Measurements are taken in the range of 10 to

300 K. Thermal losses between the cold finger and the sample holder prevented experiments below 10 K. Data was collected in 2-K increments from 10 to 50 K, 10-K increments from 50 to 120 K, and 40-K increments from 120 to 300 K. This decision was based on the change in theoretical bandgap energy of InSb as a function of temperature. However, it was determined that due to time constraints, 20-K increments would suffice.

Photoluminescence

Photoluminescence measurements consist of a laser source, two focusing lenses, a cryostat and a spectrometer (see Figure 3.6). The laser used for photoluminescence experiments is the Coherent DEOS model MID-IR 2 laser. It is a frequency doubled carbon dioxide (CO₂) laser whose wavelength output is 4.636 μm . It has an RF power supply capable of creating pulses at a rate from 10 to 130 kHz. For these experiments, the pulse rate is set to the highest capable rate, 130 kHz. A power meter is positioned in front of the laser and the modulating timer is tuned to obtain optimum output power.

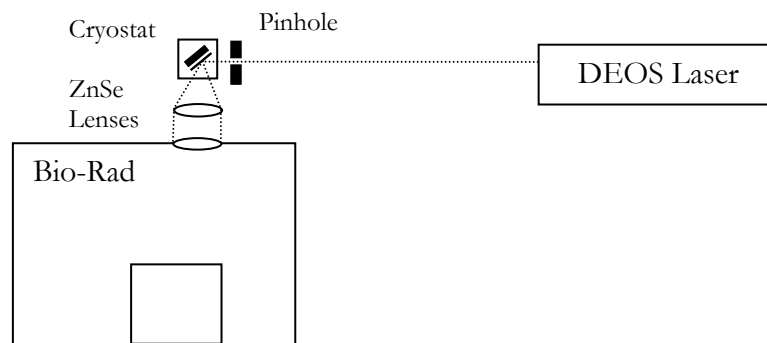


Figure 3.6. Set-up for photoluminescence experiments.

The lenses used to focus and collect sample luminescence are ZnSe plano-convex lenses with 2-inch diameters and 100-mm focal lengths. The lens nearest the cryostat

also has an antireflective coating at 4.636 μm . The spectrometer used for photoluminescence measurements is the Bio-Rad model FTS-60A. A small internal component (the aperture wheel) was changed from the absorption configuration to allow an external source. The new aperture wheel included a mirror that directed incoming external light to enter the same path as the globar source. The Helitran® Open Cycle cryogenic refrigeration system model LT-3-110 was re-positioned with windows adjacent to each other and sample holder tilted at approximately 30° to allow the interior of the cryostat to act as a beam stop, yet still allow sample luminescence to be collected by the ZnSe focusing lenses.

Light from the DEOS laser is incident upon the sample with an approximate spot size of 2 mm. Luminescence from the sample is collected by a pair of ZnSe lenses and focused into the Bio-Rad FT-IR spectrometer. Similar to the absorption measurements, a background measurement is taken first; however, for photoluminescence experiments, the background measurement is a scan with the laser blocked. The scan-type is “Raman-scan”, which tells the software to configure Bio-Rad to accept an external source from the back of the system, similarly to the configuration for Raman spectroscopy. The background is subtracted from each measurement. The sample is again cooled using liquid helium. Measurements are taken in the range of 20 to 160 K with laser power ranging 28 mW to 1.43 W.

Variable Temperature Resistivity

Variable Temperature Hall measurements were performed by Tim Cooper of the Sensors Branch of the Hardened and Sensor Materials Division in the Materials and

Manufacturing Directorate of the Air Force Research Lab (AFRL/MPLS). Indium contacts were soldered on the four corners of each sample. Resistivity measurements were taken at temperatures ranging from 20 to 317 K. Conductivity, the inverse of resistivity, is related to activation energies by:

$$\sigma = Ae^{\frac{-E_{activation}}{k_B T}}, \quad (38)$$

where E_a is activation energy and \mathcal{A} is a constant. The conductivities were modeled as a function of inverse temperature.

3.5 Summary

Absorption and photoluminescence are both performed using the Bio-Rad FT-IR spectrometer with slightly differing setups. Optical sources include the globar ceramic lamp for absorption and the DEOS frequency doubled CO₂ laser for photoluminescence. The sample is cooled in both experiments using liquid helium as the refrigerant in the Helitran Open Cycle cryostat. Absorption measurements are taken in the range of 20 to 300 K in 20-K increments. Photoluminescence measurements are taken in the range of 22 to 160 K with laser power ranging 28 mW to 1.43 W.

IV. Results and Discussion

4.1 Chapter Overview

This chapter presents the results obtained from the experiments described in Chapter 3. Experimental results discussed include those from absorption and photoluminescence measurements. Also included are variable-temperature resistivity measurements taken by Tim Cooper at AFRL/MLPS.

4.2 Absorption

Bare Indium Antimonide

Absorption measurements were taken on samples at different locations on the wafer. Figure 4.1 shows the absorptance at 80 K for measurements taken at the edge and center of the wafer. As temperature increased, the absorption edge decreased as expected. As discussed in Chapter 2, the bandgap decreases with increasing temperature. The absorption coefficient is proportional to the optical joint density of states. This implies that as temperature is increased, the absorption threshold energy should decrease as is seen in Figure 4.2.

The theoretical absorption coefficient was modeled using Equation (36) and the measured absorption coefficient was calculated using Equation (35). When compared to the theoretical absorption coefficient, it becomes clear that as temperature increases, the absorption edge lies below what is expected (see Figure 4.3). A peak just below the theoretical bandgap energy forms and increases in intensity as temperature increases. This peak is probably due to a shallow impurity state. For a shallow acceptor state, as

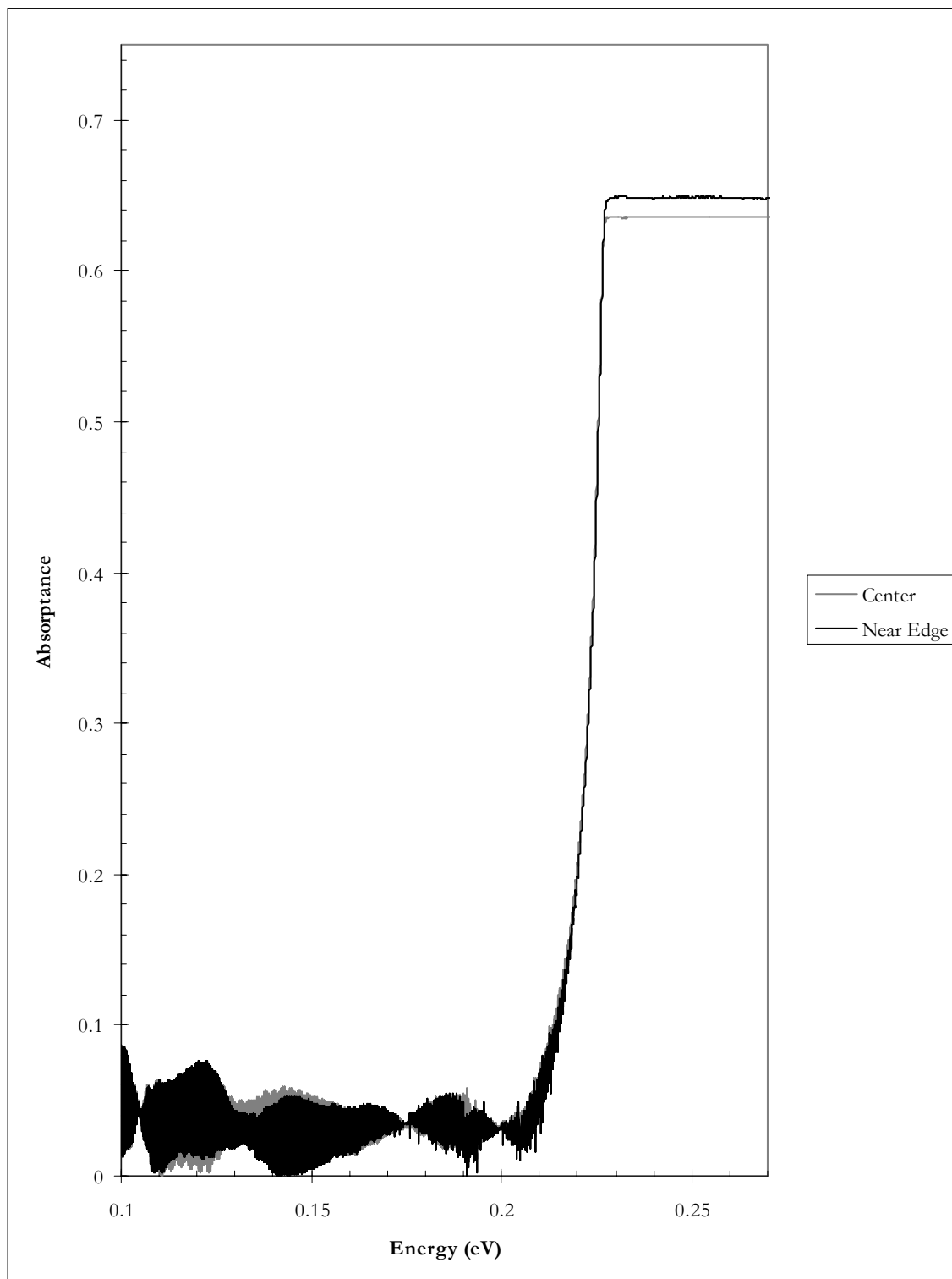


Figure 4.1. Absorbance near the edge and center of the bare InSb wafer at 80 K.

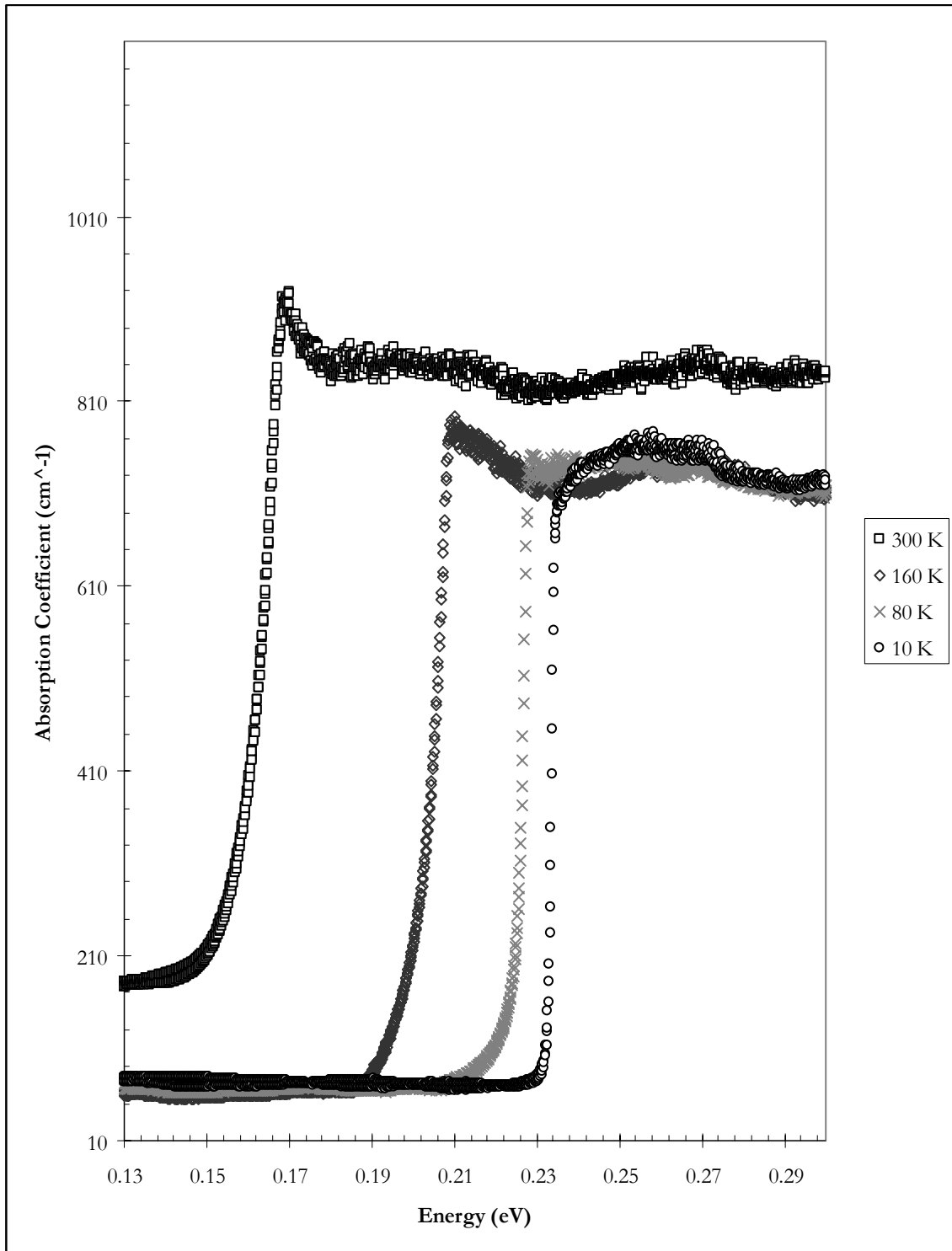


Figure 4.2. Absorption coefficient as a function of temperature for bare InSb at 300 K (\square), 160 K (\diamond), 80 K (\times), and 10 K (\circ).

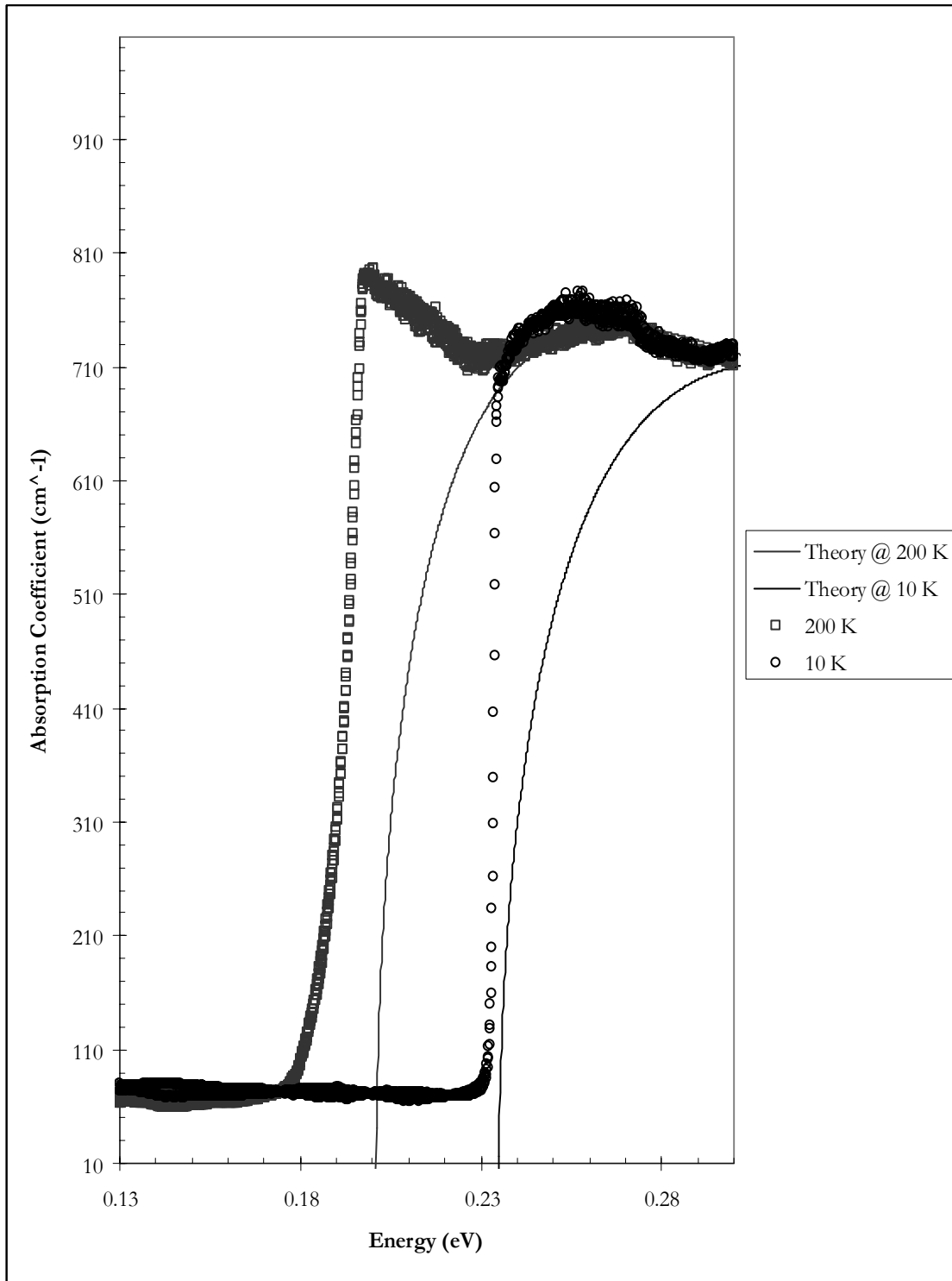


Figure 4.3. Comparison of theoretical absorption coefficient of bare InSb to the measured absorption coefficient at 10 K and 200 K.

temperature increases, more electrons are thermally excited into the acceptor state. The energy difference between the acceptor level and the conduction band is less than the bandgap, allowing a peak in the absorption to occur at less energy than the bandgap. This is similar for shallow donor states and valence-band-to-donor transitions or acceptor-to-donor-transitions.

Anodized Indium Antimonide

Absorption measurements were again taken on the anodized samples at different locations on the wafer. Figure 4.4 shows the absorptance at 80 K for measurements taken at the edge and center of the anodized wafer. Note the small peak at 0.133 eV.

Figure 4.5 shows the absorption coefficient of the center sample as a function of several temperatures and a close-up of the peak, itself. Unlike the absorption threshold (that closely follows trends of the bare InSb), the unknown peak does not appear to vary with temperature. Interestingly, this is the exact photon energy of the fundamental transition of the 9.272- μm DEOS laser used in the photoluminescence measurements. There is no explanation for why this transition would be seen in the absorption measurements.

SiO_x on Indium Antimonide

Absorptance measurements taken at different locations on the wafer are shown in Figure 4.6. Figure 4.7 shows the absorption coefficient at different temperatures of the center sample. The SiO_x-on-InSb sample had a very noticeable ‘bump’ in the absorption spectra. This small region of low absorption was observable at all

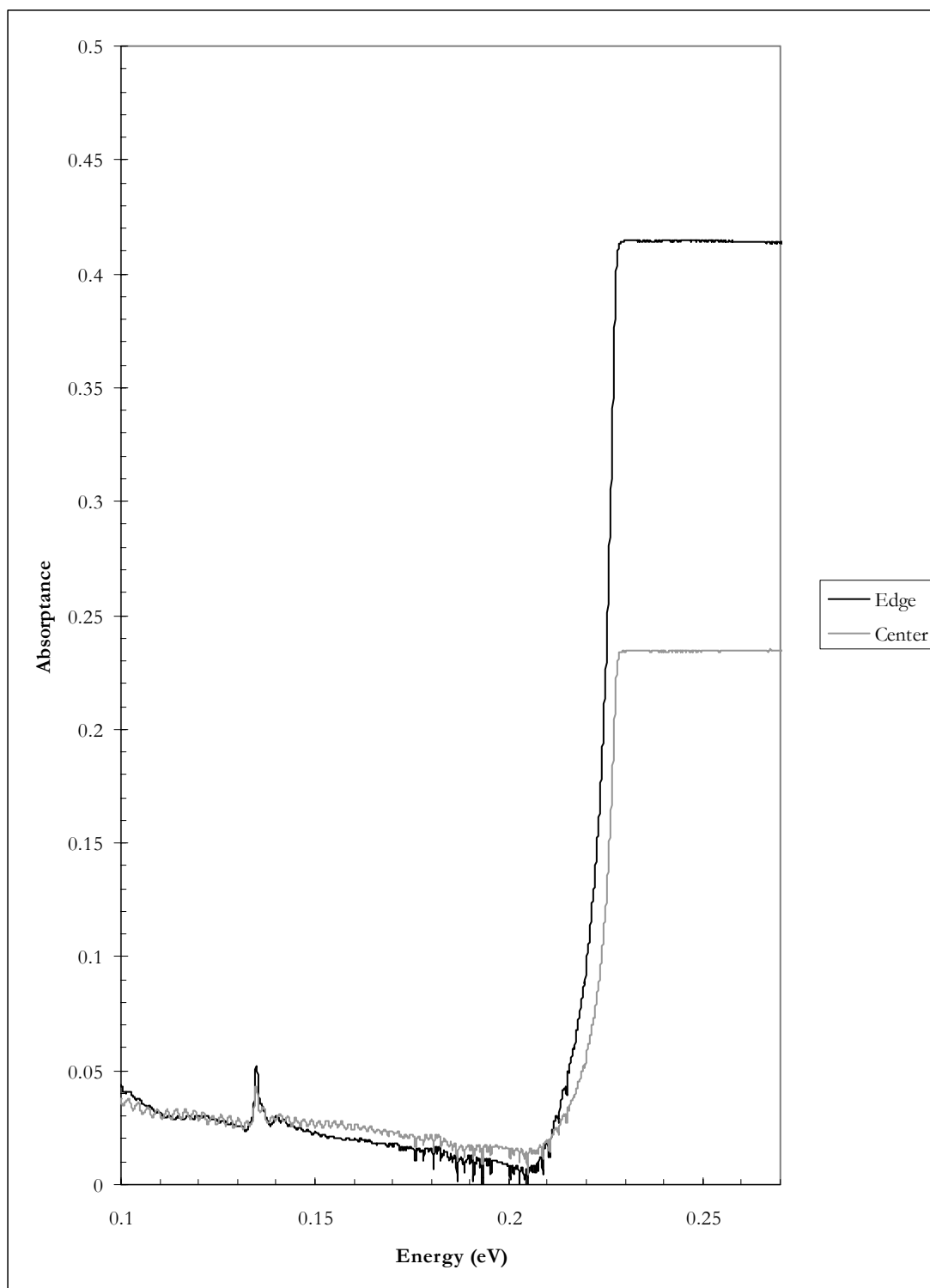


Figure 4.4. Absorptance of edge and center of anodized InSb wafer.

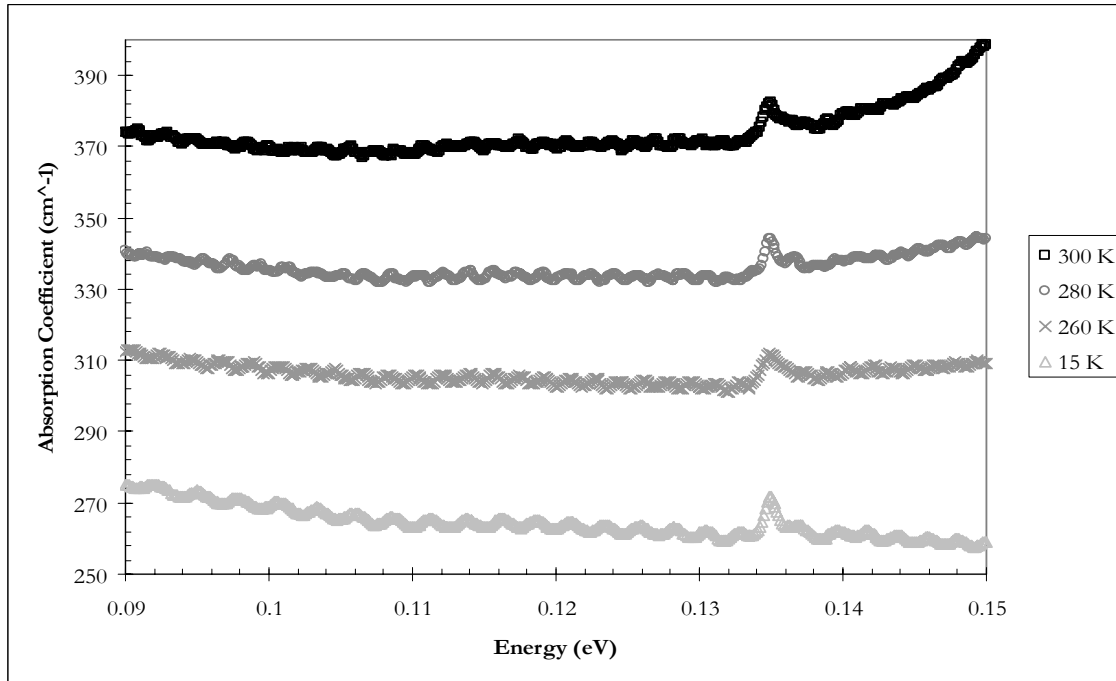
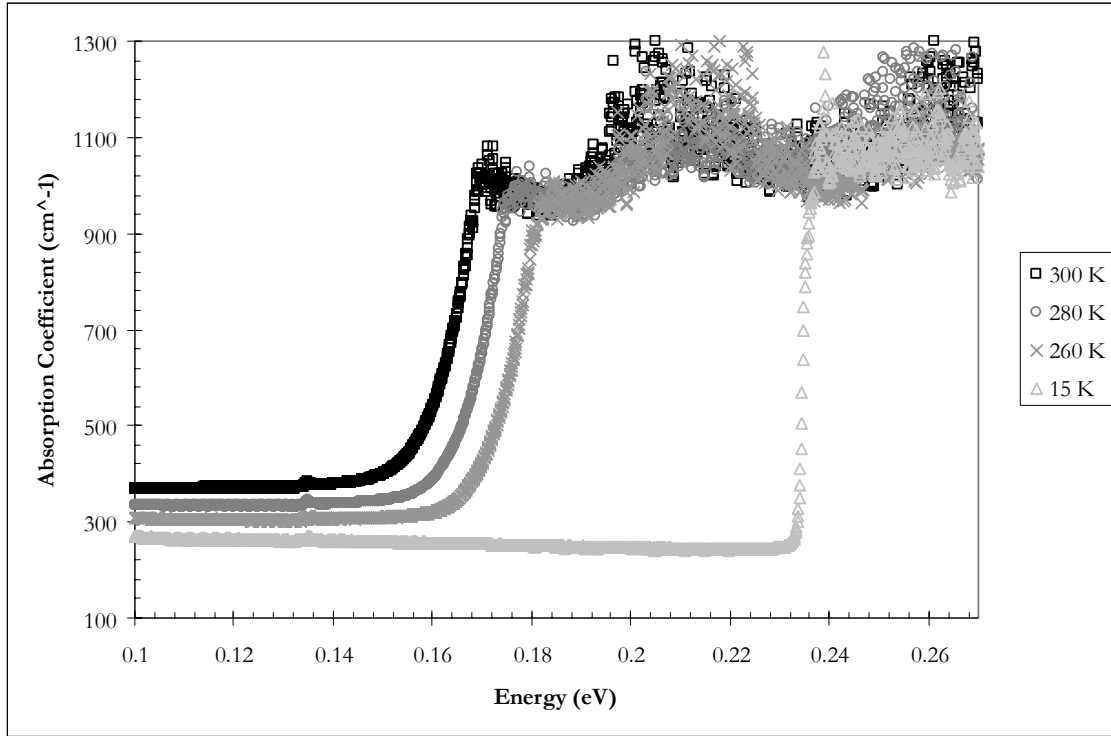


Figure 4.5. Impurity absorption of anodized InSb at the center of the wafer at 300 k (\square), 280 K (\circ), 260 K (\times), and 15 K (Δ).

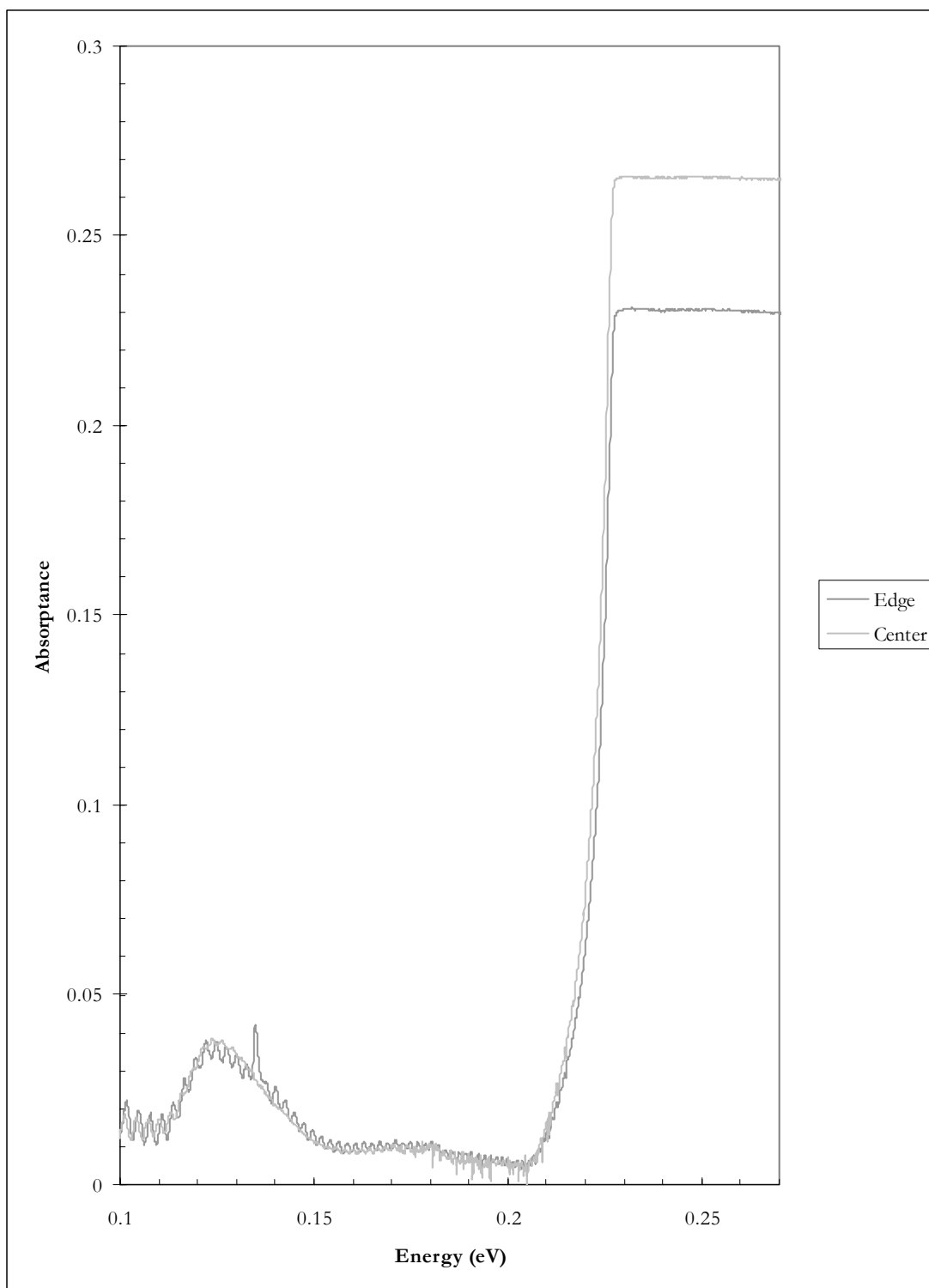


Figure 4.6. Absorbance of edge and center of SiO_x on InSb

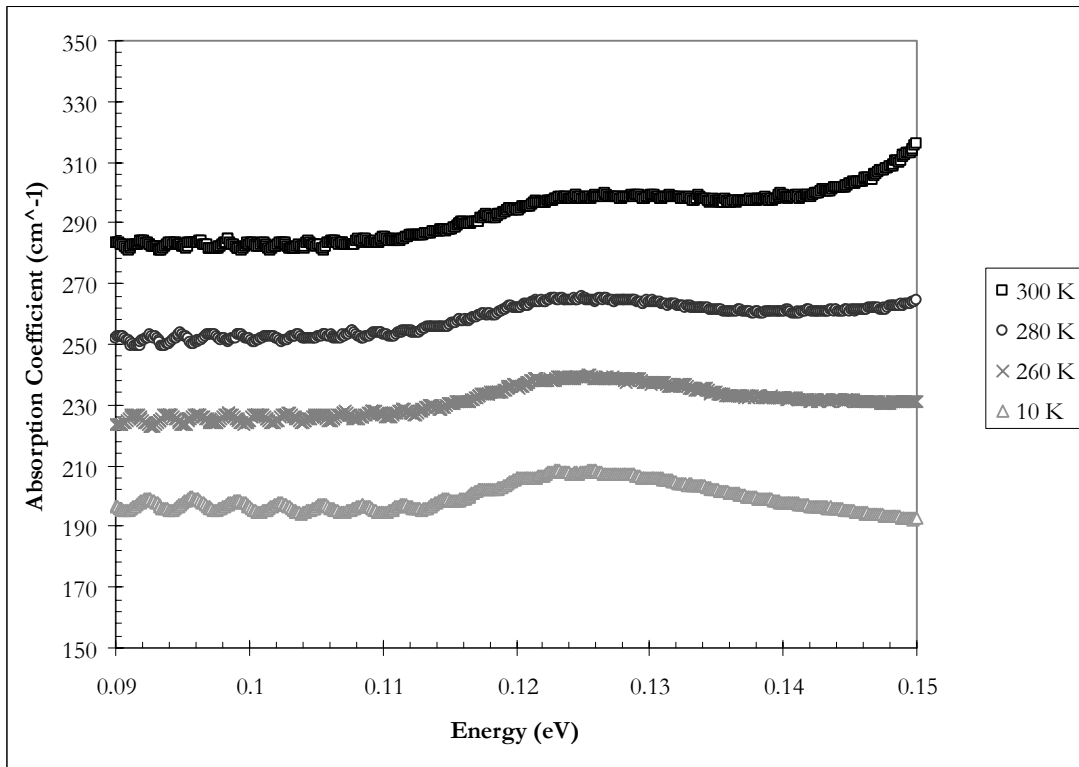
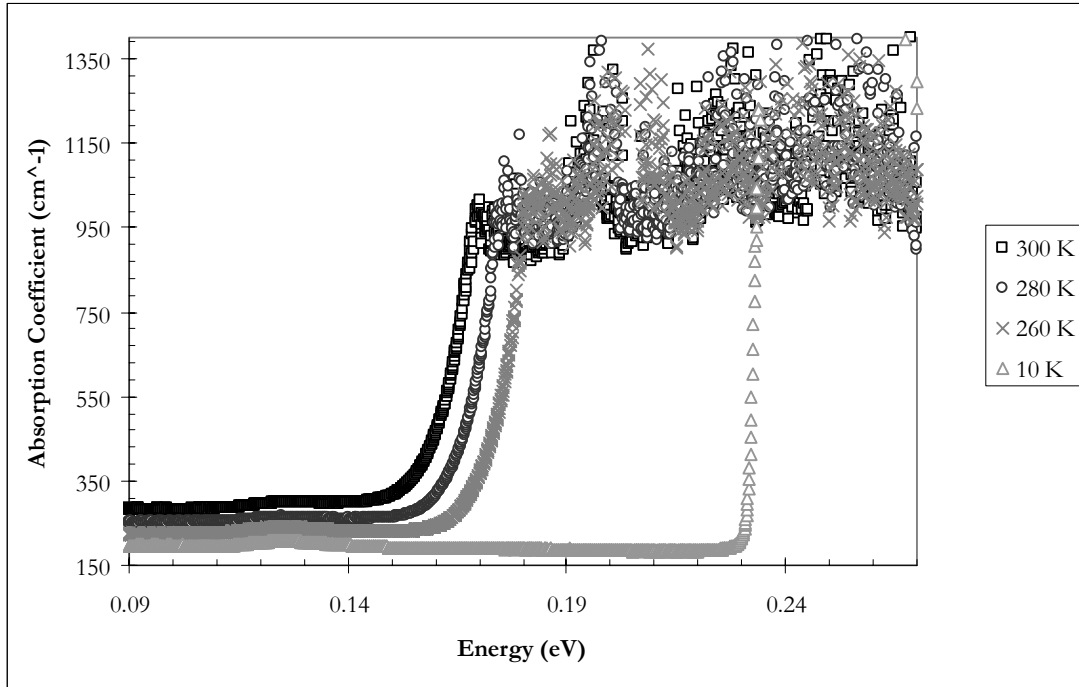


Figure 4.7. Impurity absorption of SiO_x-on-InSb at the center of the wafer at 300 k (□), 280 K (○), 260 K (×), and 10 K (Δ).

temperatures and, similarly to the anodized InSb, it does not appear to shift with temperature changes. The increase in absorption begins around 0.114 eV with a peak at 0.125 eV. At room temperature, the band tail of the absorption threshold begins to merge with this peak.

Absorptance Comparison

Figure 4.8 shows the 80-K absorptance spectra of the Bare, Anodized, and SiO_x-on-InSb. The dashed vertical line represents the theoretical bandgap energy. The unknown absorption peak only appears in the SiO_x-on InSb and anodized InSb samples. However, the width of the unknown SiO_x peak does encompass the anodized sample's unknown peak. The periodic trend in absorptance below the absorption threshold could be due to a Fabry-Perot effect. However, since the effect is greater in the bare sample than in the passivated samples, this is unlikely.

4.3 Photoluminescence

Photoluminescence was taken using the Bio-Rad FT-IR spectrometer. Many of the peaks in the spectra were inverted or partly inverted. A negative signal makes no sense physically. The negative values are probably due to the Bio-Rad's Fourier transform process. It should be noted that the absolute values were taken of all photoluminescence spectra reported herein.

Bare Indium Antimonide

A peak in the photoluminescent spectra was observed near the band edge for the bare InSb sample. Figure 4.9 is an overlay plot of the 22-K photoluminescence and

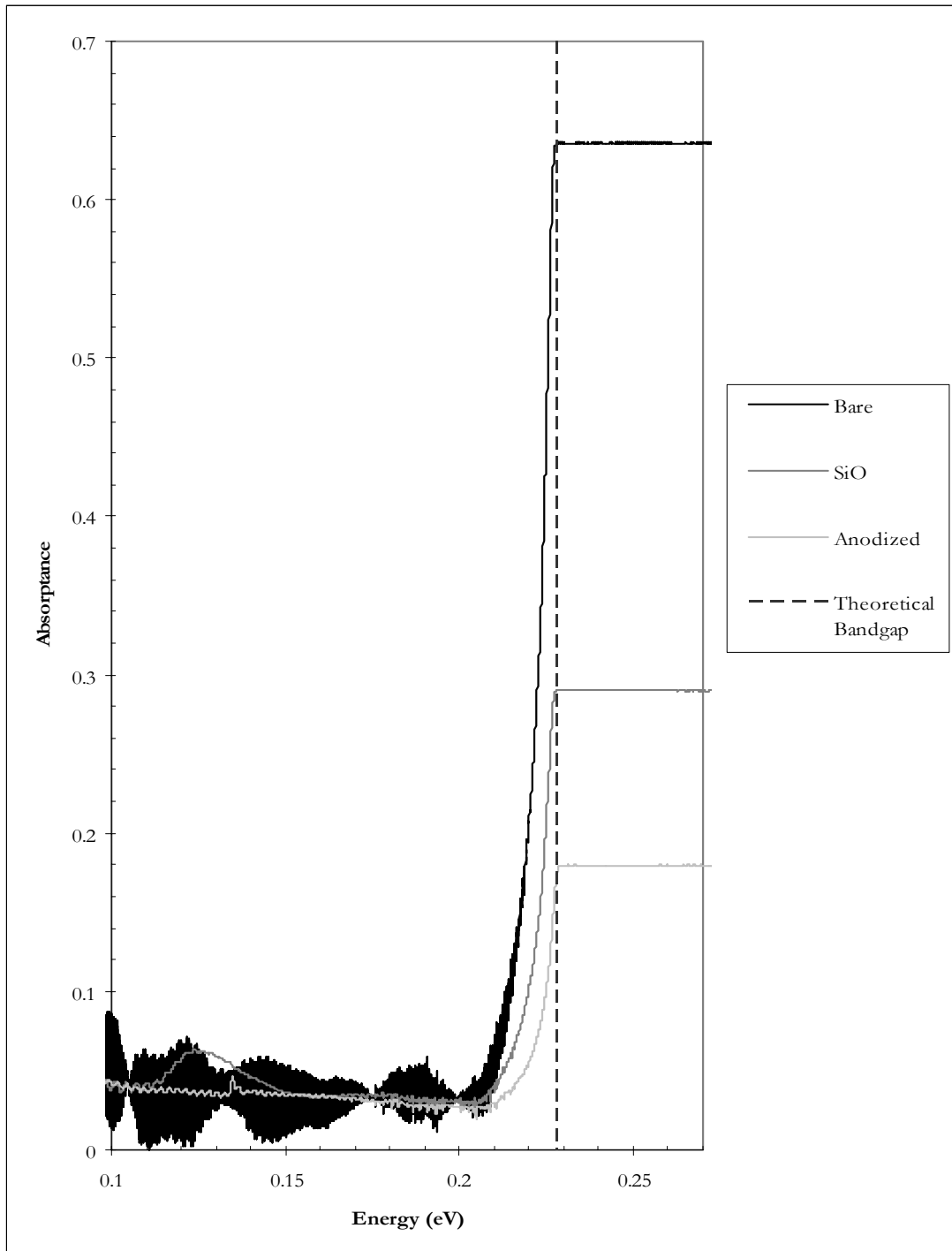


Figure 4.8. Absorbance at 80 K of InSb, anodized InSb and SiO on InSb. The dashed line is the theoretical bandgap energy.

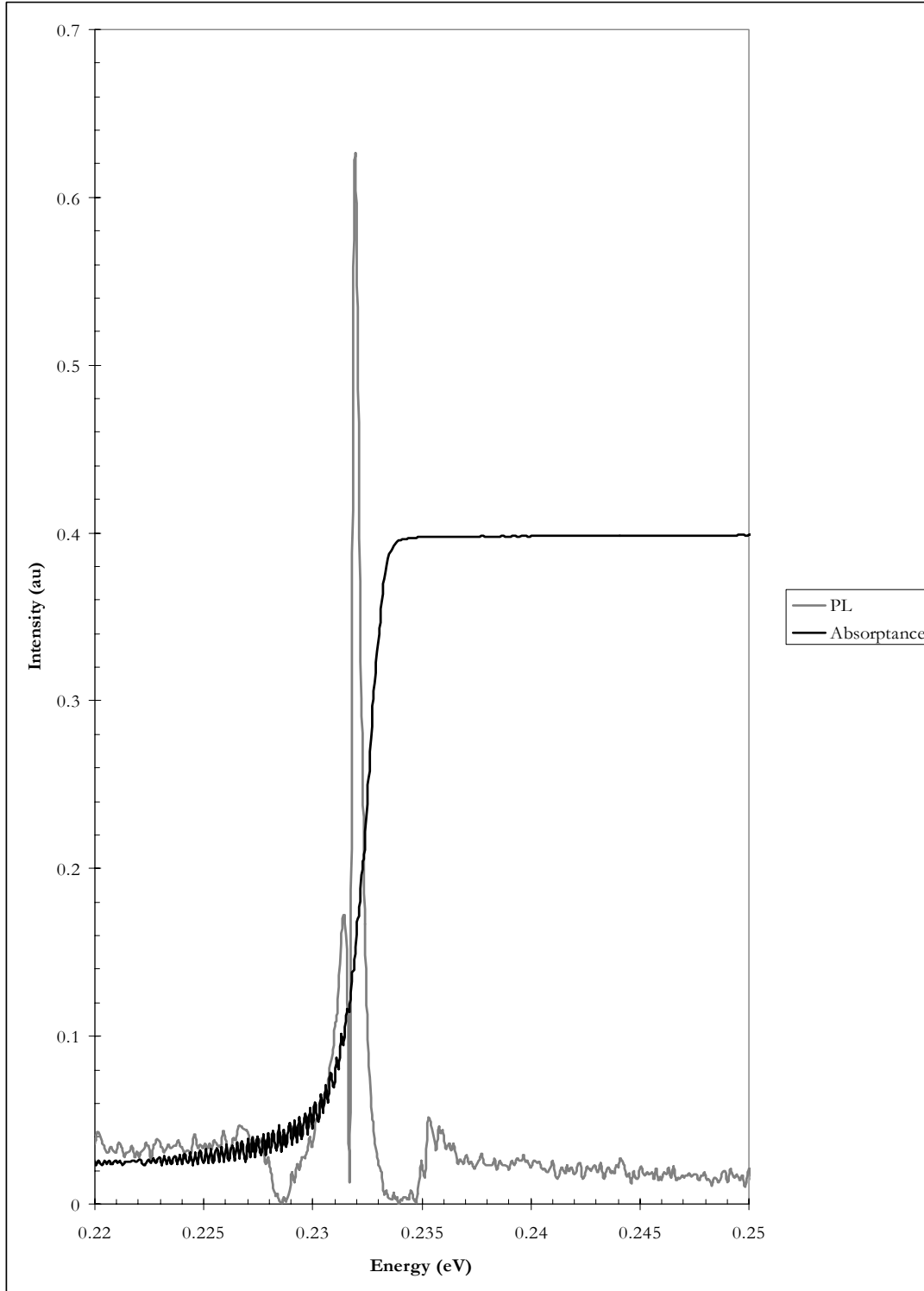


Figure 4.9. Overlay plot of photoluminescence and absorbance spectra of bare InSb at 22 K . The photoluminescence peak is at 0.232 eV. The theoretical bandgap energy is 0.234 eV.

absorptance spectra. The photoluminescent peak is at 0.2322 eV, only 2.24 meV less than the theoretical bandgap. This is typical as excited electrons will relax into donor states before radiatively recombining with holes in the valence band, or may transition into acceptor states.

As the pump power was increased, the intensity of the photoluminescence peak increased, as shown in Figure 4.10. The dip in the peak is a result of the absolute value being taken on a spectrum that flipped to the negative. It is not believed to be a real second peak. On the contrary, as temperature increased, the peak began to decrease and then disappeared at 26 K (see Figure 4.11). The peak at 24 K is observed at 0.23145 eV, 2.89 meV below the theoretical bandgap energy of 0.23434 eV. No peak was observed at 0.232 eV for temperatures above 26 K.

Anodized Indium Antimonide

No photoluminescent peak was observed at or near the bandgap energy for the anodized InSb. A peak was, however, observed at 0.1336 eV, which is the fundamental transition of the DEOS laser at 9.272 μm . (This is the same position as the unknown peak observed in the absorption spectrum.) The unknown peak increased with optical pump power as is seen in Figure 4.12. Figure 4.13 shows an overlay plot of photoluminescence and absorptance at 80 K. Also seen in this plot is the laser line at 0.267 eV. The magnitude of this line and subsequent saturation of the DTGS detector could be the cause of the partly inverted photoluminescence peaks in the Fourier-transform process.

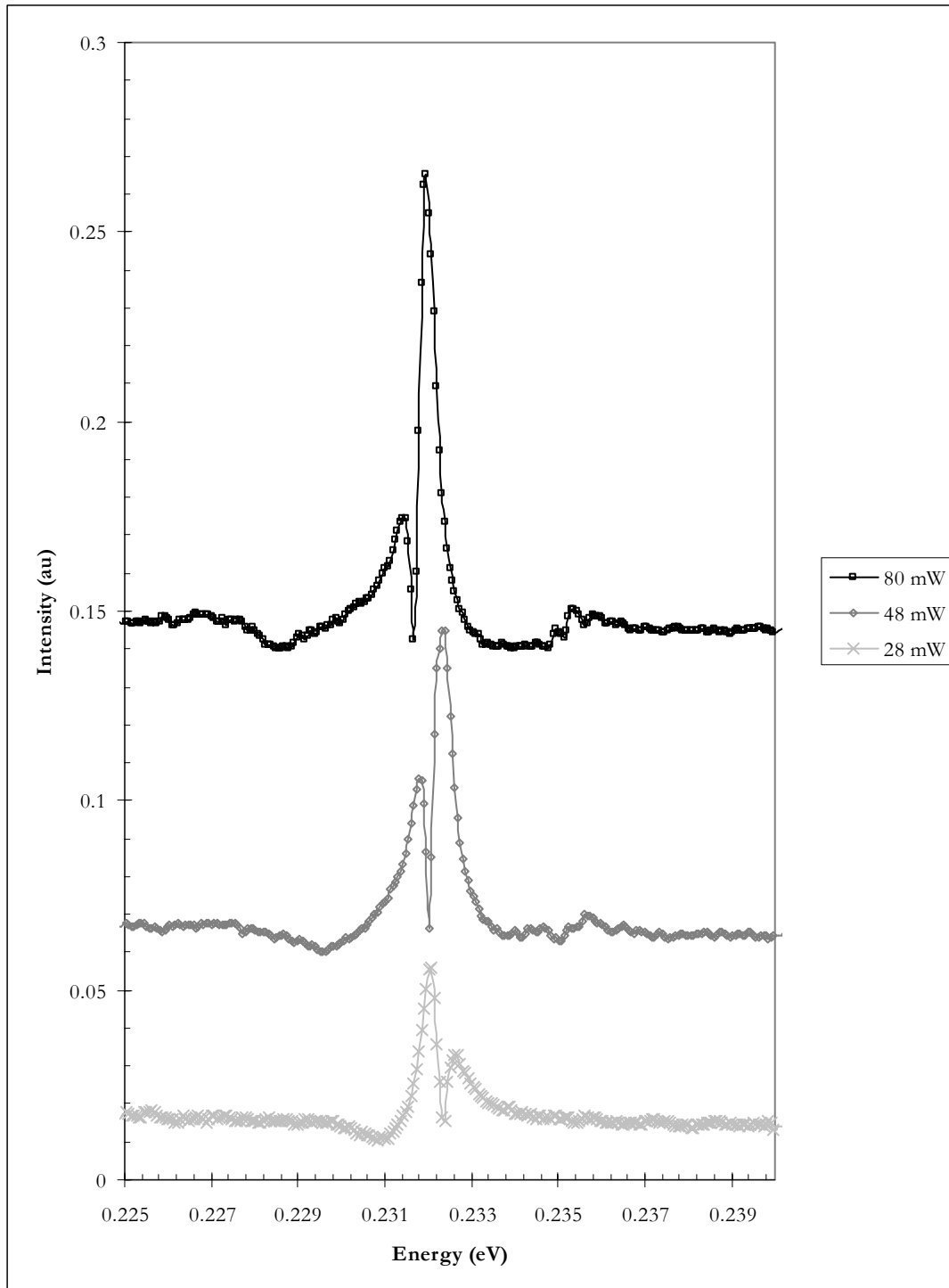


Figure 4.10. Photoluminescence of bare InSb taken at 22 K with increasing optical pump powers: 28 mW, 48 mW, and 80 mW.

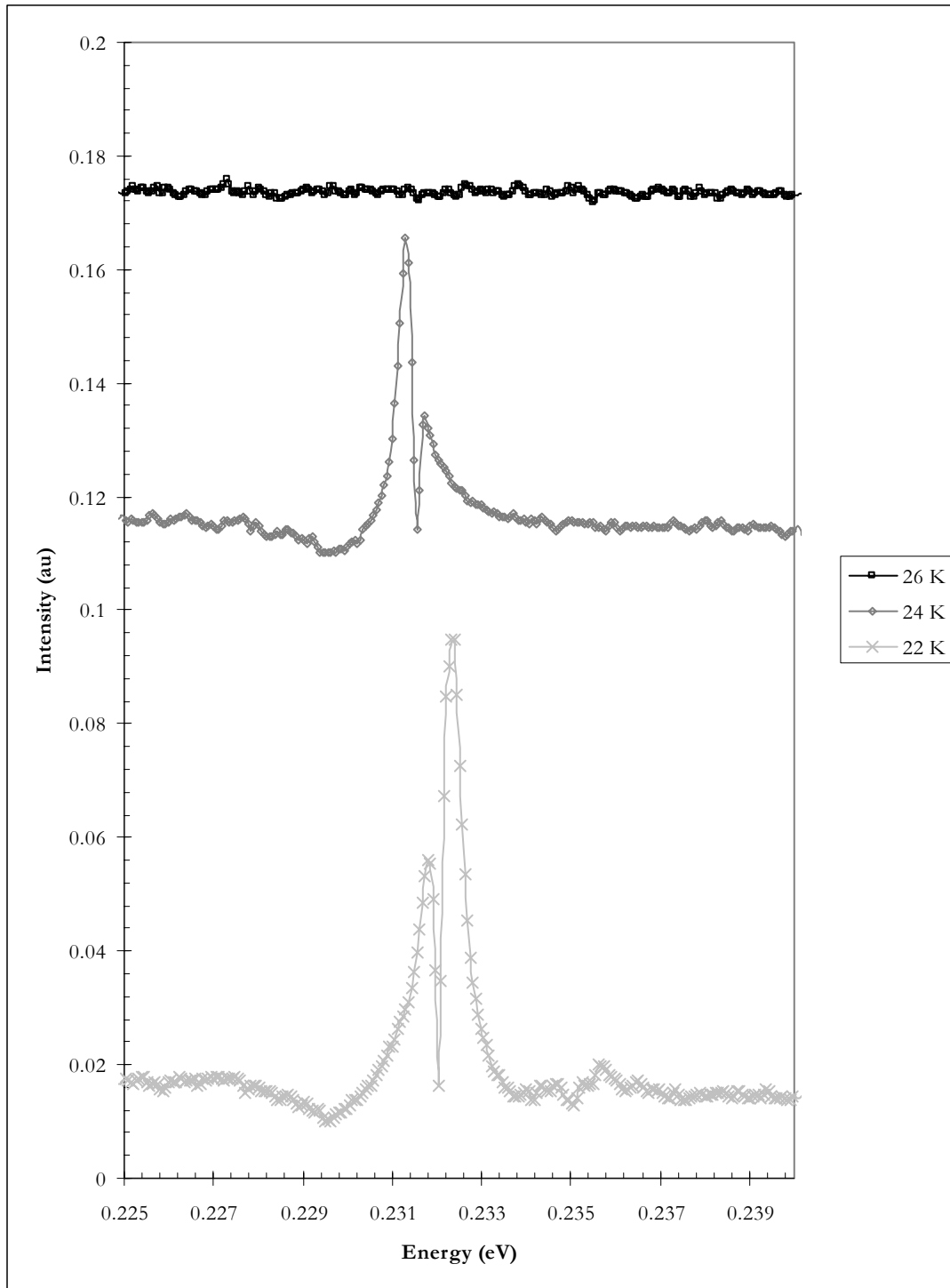


Figure 4.11. Photoluminescence of bare InSb taken with 80 mW optical pump power at temperatures: 22 K, 24 K, and 26 K.

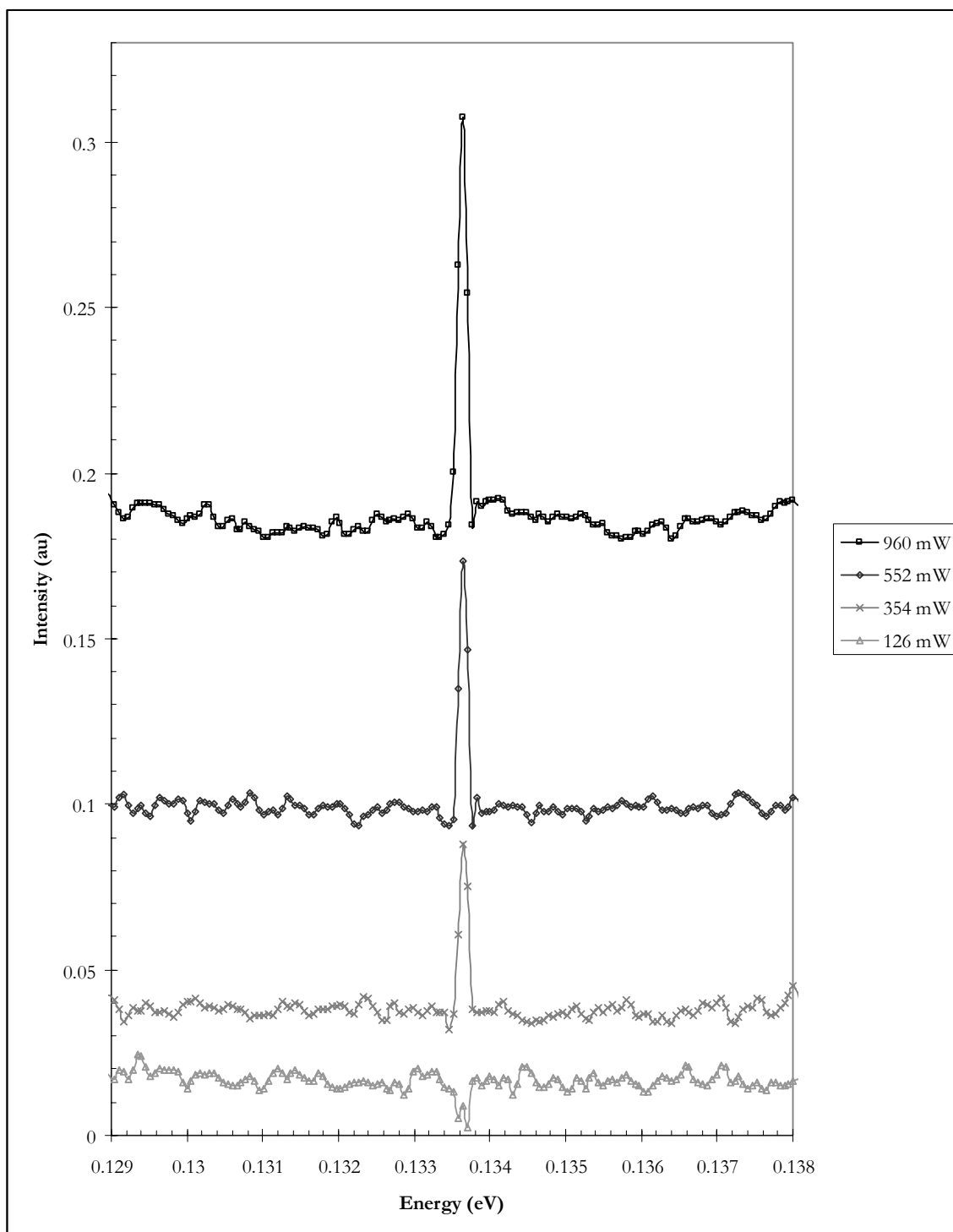


Figure 4.12. Photoluminescence anodized InSb taken at 22 K with increasing optical pump powers: 126 mW, 354 mW, 522 mW, and 960 mW.

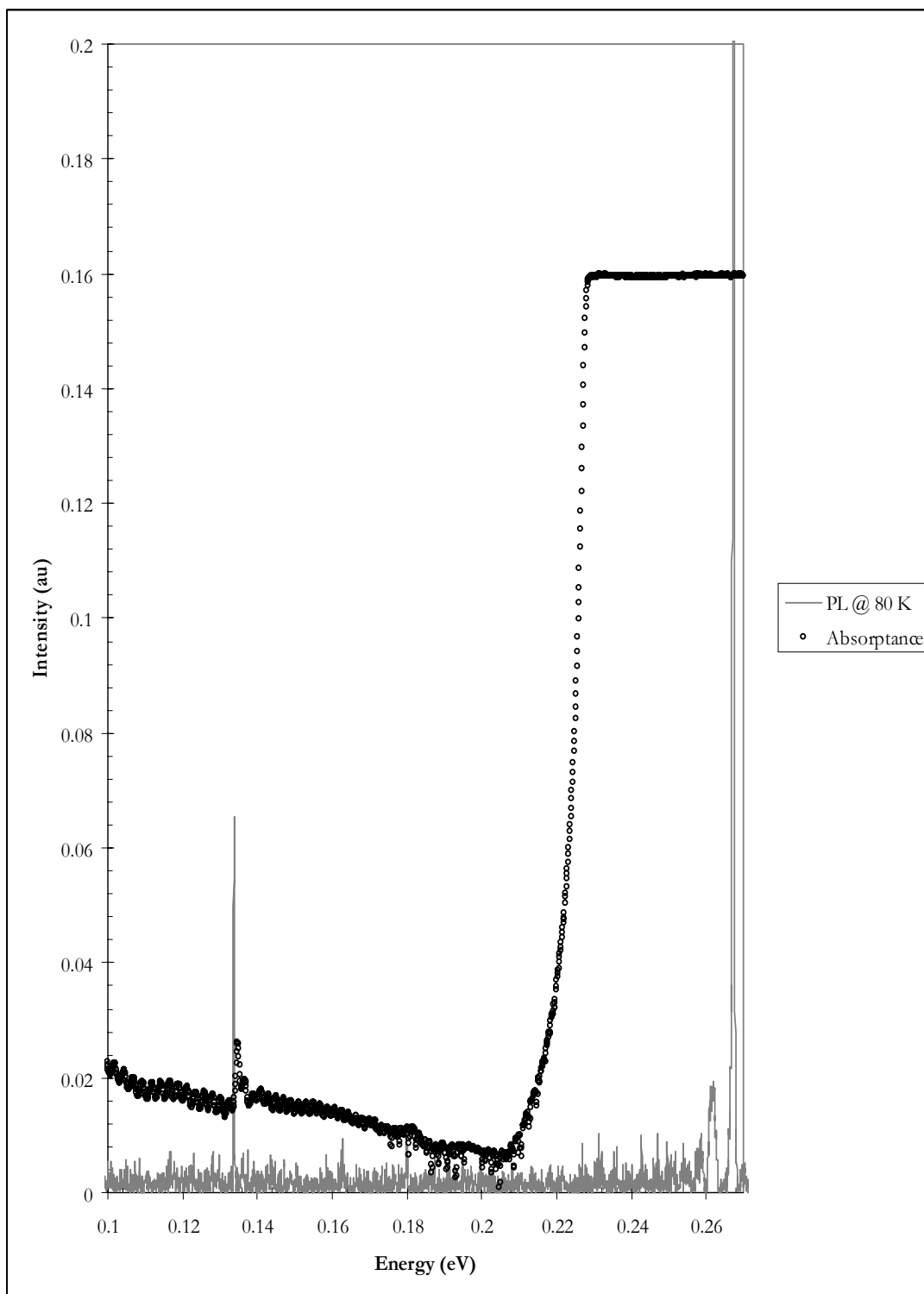


Figure 4.13. Overlay plot of impurity peak absorbance and photoluminescence for the anodized InSb sample at 80 K.

SiO_x on Indium Antimonide

Again, no photoluminescent peak was observed at or near the bandedge for the SiO_x-on-InSb sample. Figure 4.14 is an overlay plot of the photoluminescence and absorbance at 80 K. The luminescent peak is again observed at 0.1336 eV. Figure 4.15 shows the increase in photoluminescent intensity as pump power is increased. The intensity of the peak increases as is expected.

Unlike the anodized unknown peak, other peaks near the 0.1336-eV line formed as temperature was increased (see Figure 4.16). At around 26 K, two other peaks became activated. Figure 4.17 shows the lower energy sub-peak whose intensity peaks around 0.132 eV. The peak does not appear at 22 K. However, with larger temperature, the peak increases. Figure 4.18 is a close-up of the higher energy peak, located at about 0.1352 eV. Again, notice that the peak is unobservable at 22 K, yet is activated by 26 K. Although not shown in these plots, the intensity of the peaks begins to decrease again around 160 K. As with the 0.125-eV “bump” in the SiO_x-on-InSb absorption spectra, because these peaks do not shift with temperature as they would for semiconductor energetic transitions, they are difficult to explain.

4.4 Variable Temperature Hall Measurements

Bare Indium Antimonide

Figure 4.19 shows a plot of conductivity as a function of inverse temperature for the bare InSb sample. The y-axis is on a log scale. The conductivity appears to have two separate activation energies. An Excel trendline was fit to the two regions. Activation

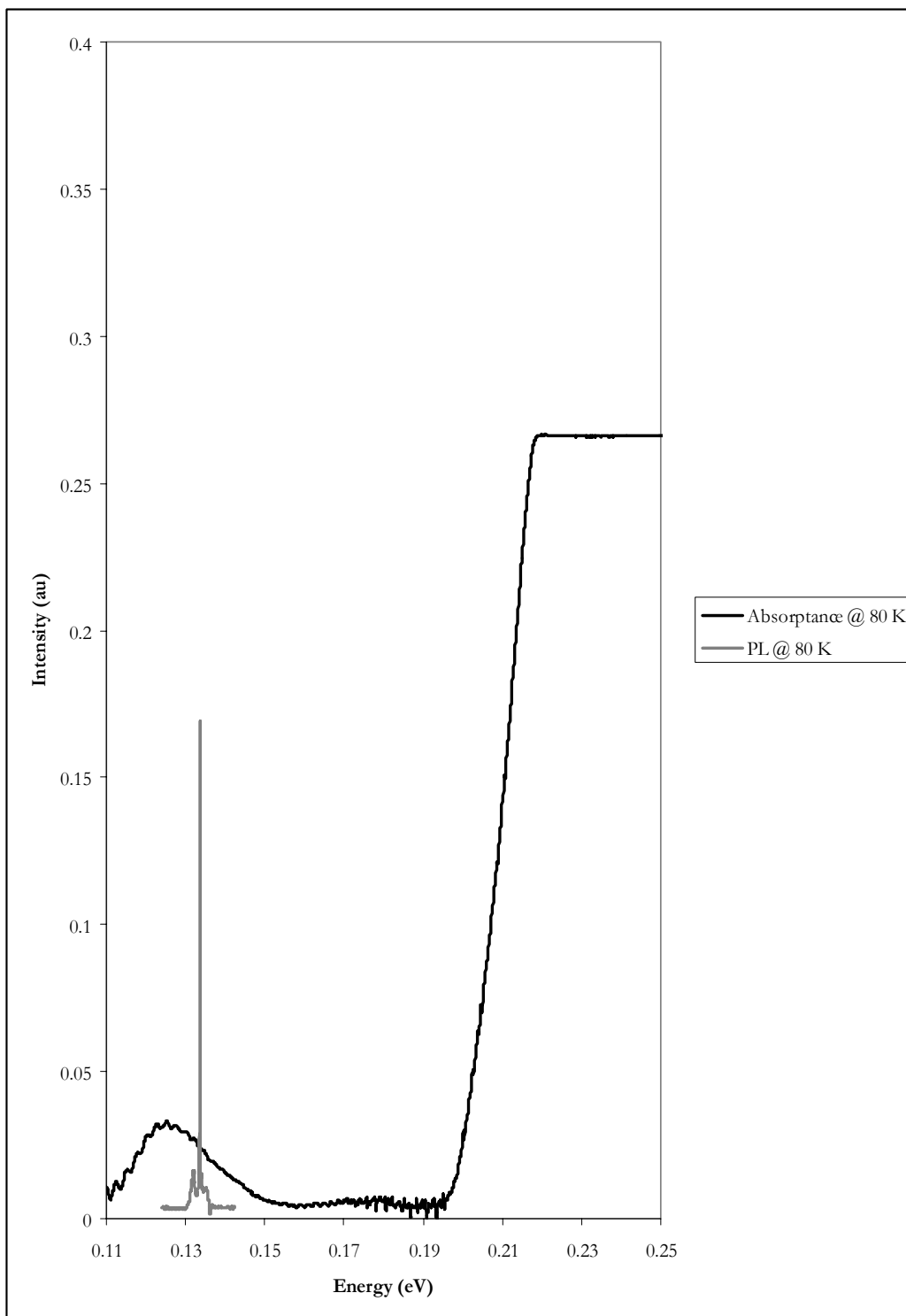


Figure 4.14. Overlay plot of impurity peak absorbance and photoluminescence for the SiO_x-on-InSb sample at 80 K.

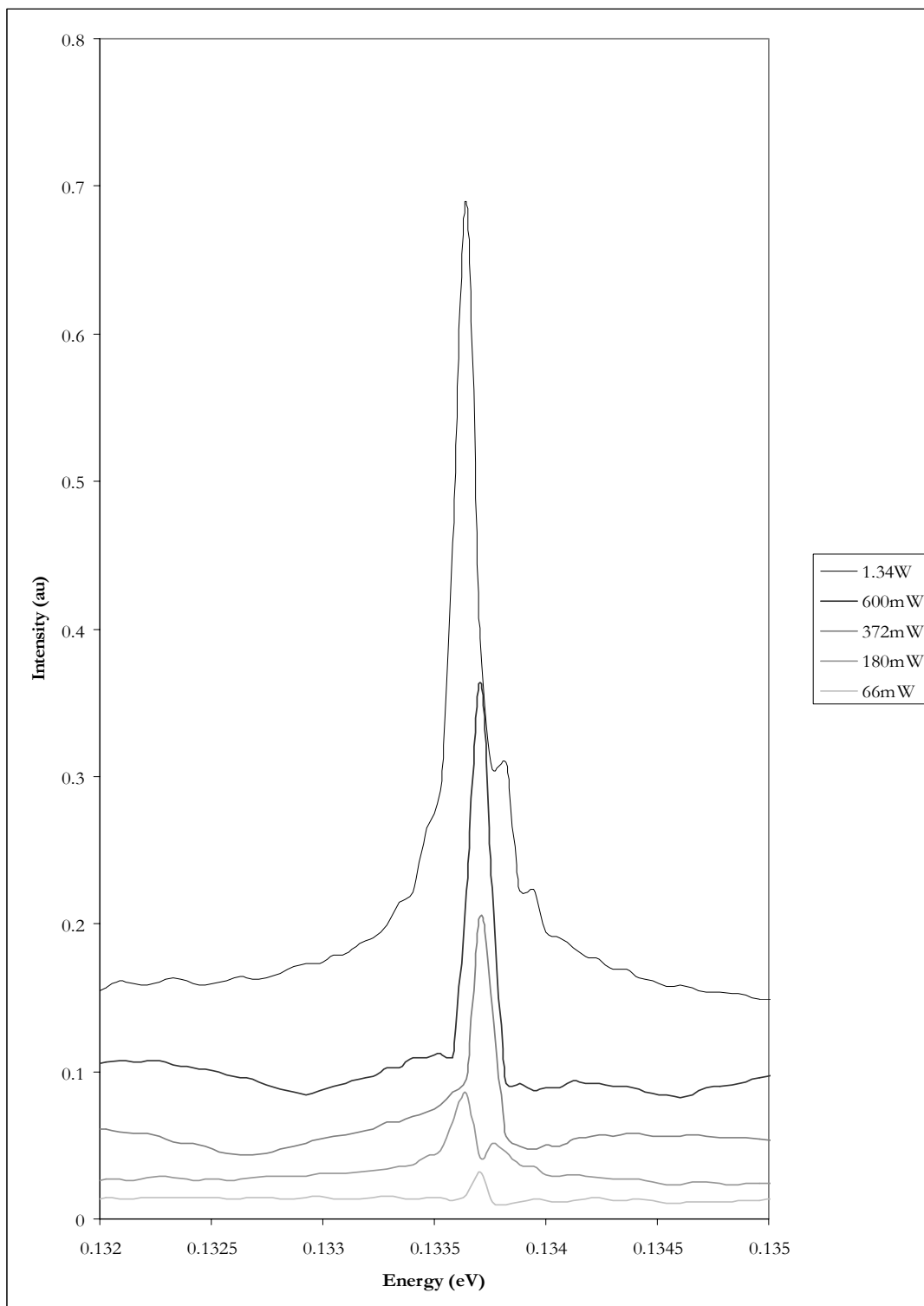


Figure 4.15. Photoluminescence of SiOx-on-InSb taken at 20.5 K with increasing optical pump powers: 66 mW, 180 mW, 372 mW, 600 mW, and 1.34 W.

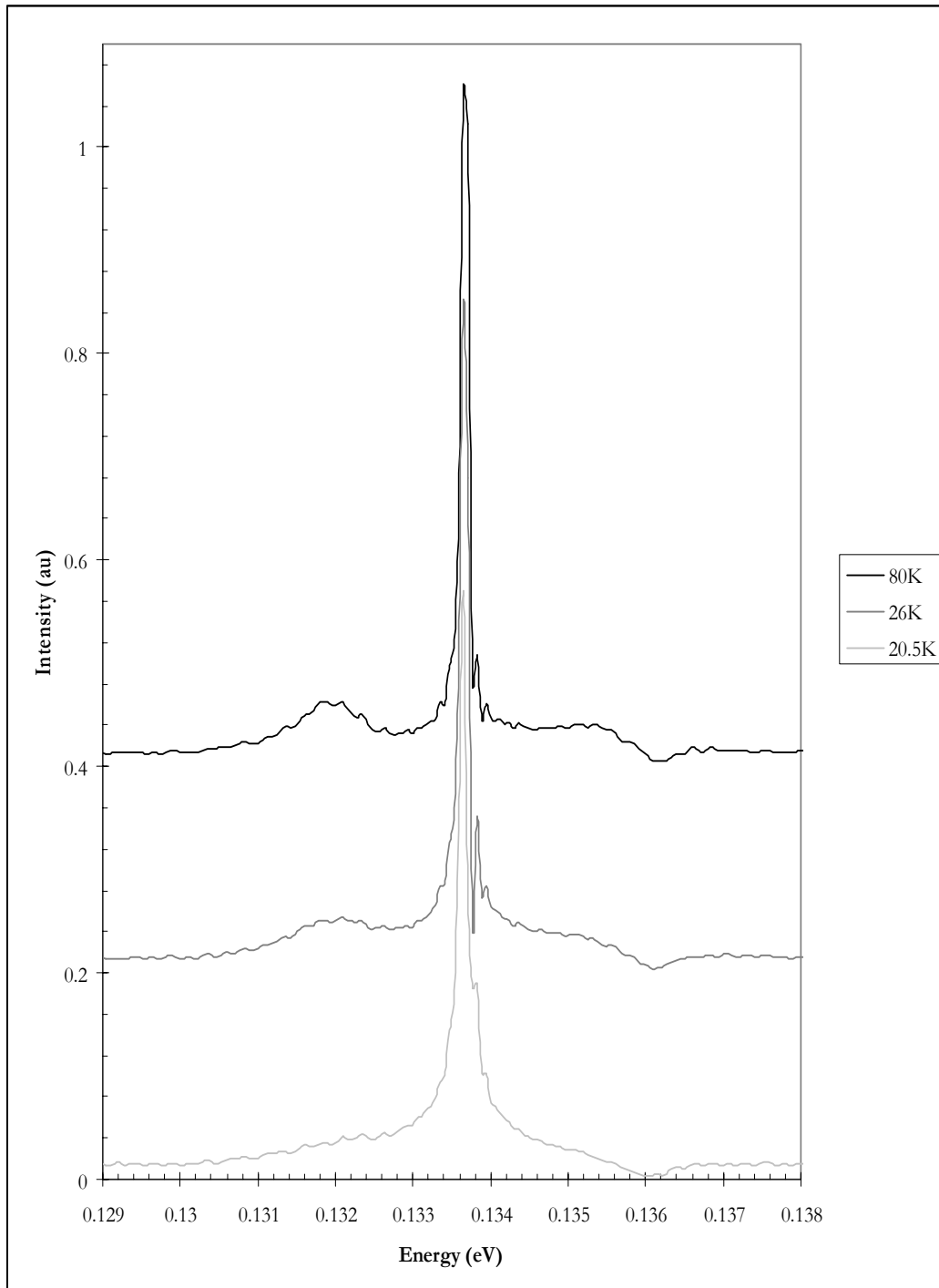


Figure 4.16. Photoluminescence of SiO_x-on-InSb taken with an optical pump power of 1.34 W at temperatures of 20.5 K, 26 K, and 80 K.

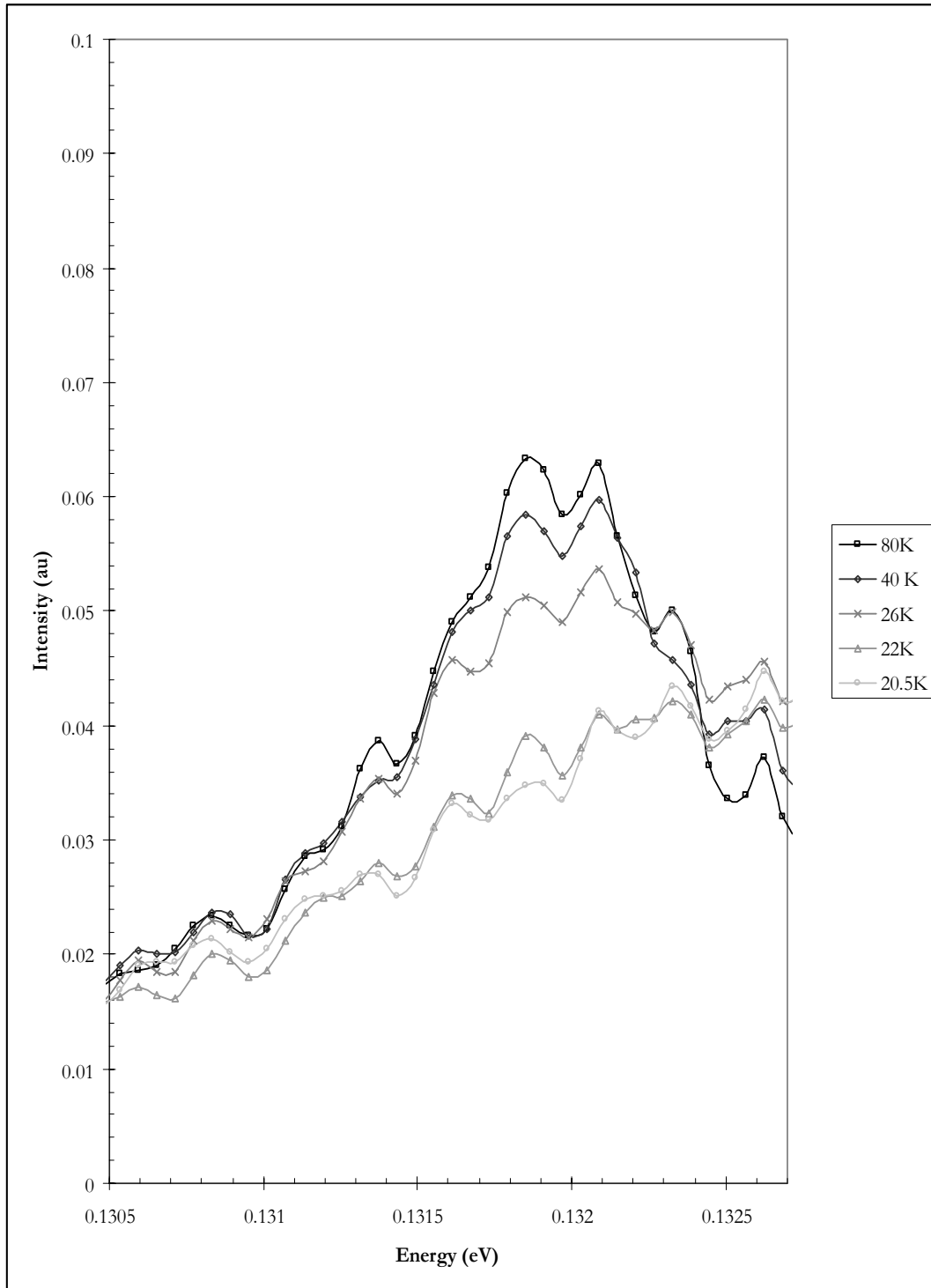


Figure 4.17. Lower energy sub-peak of main photoluminescence peak of SiO_x-on-InSb. Optical pump power is 1.34 W and curves represent measurements taken at 20.5 K, 22 K, 26 K, 40 K and 80 K.

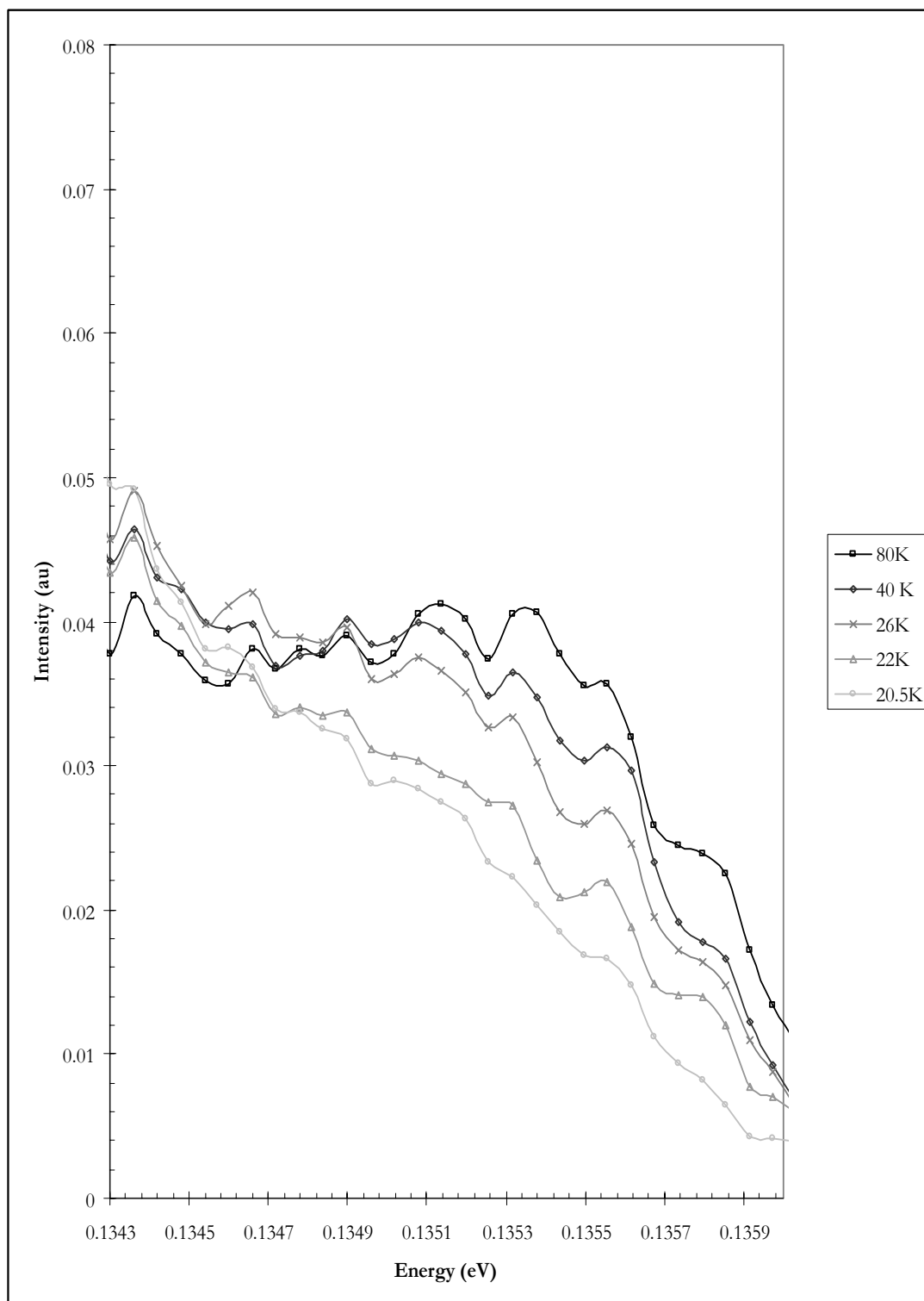


Figure 4.18. Higher energy sub-peak of main photoluminescence peak of SiO_x-on-InSb. Optical pump power is 1.34 W and curves represent measurements taken at 20.5 K, 22 K, 26 K 40 K and 80 K

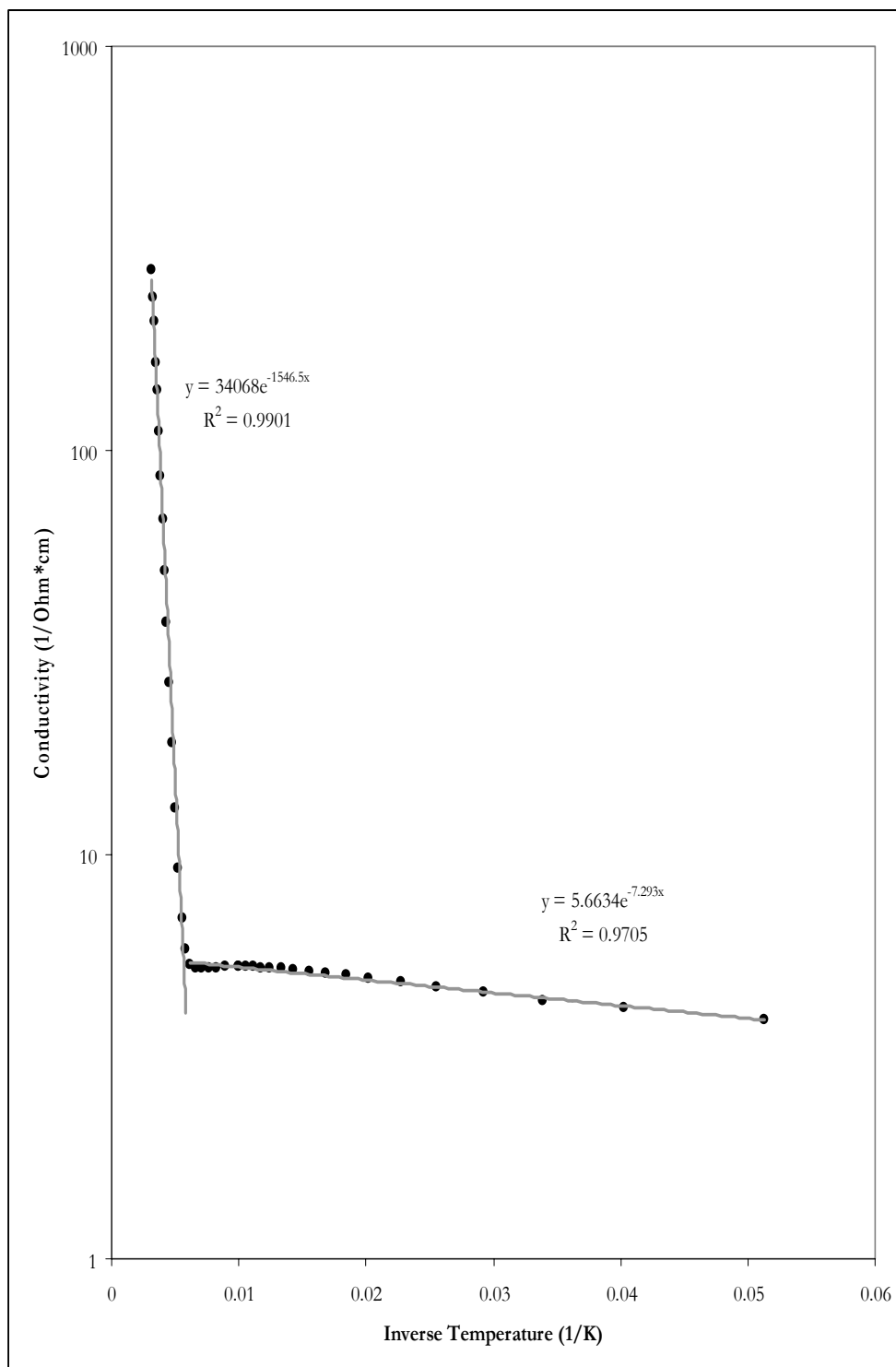


Figure 4.19. Conductivity of InSb as a function of inverse temperature. The higher and lower temperature realms have been fitted with separate exponential curves.

energies of 0.13326 eV and 0.628 meV were determined. The fact that the larger activation energy is the about the same as the photon energy of the fundamental 9.272- μm DEOS laser line is just a coincidence. Madelung (2004) reports that “shallow, effective-mass like donors are always present in concentrations of at least 10^{13} cm^{-3} . [They have] a small binding energy of 0.7 meV.” The carrier concentration was $7.96 \times 10^{14} \text{ cm}^{-3}$ at 20 K, making it likely that the smaller activation energy is due to the shallow, effective-mass like donors.

SiO_x on Indium Antimonide

Variable-temperature resistivity measurements were also performed on the SiO_x - on-InSb samples. Figure 4.20 is the plot of conductivity versus inverse temperature. Again, two exponentials were used to fit the data. Activation energies for the SiO_x-on-InSb sample were 0.1327 eV and 0.745 meV. Again, the larger activation energy seems to coincidentally correspond to the DEOS laser fundamental photon peak energy observed in absorbance and photoluminescence spectra. The shallow, effective-mass like donors again are present.

Anodized Indium Antimonide

Resistivity measurements were attempted on the anodized InSb. However, the anodization provided an excellent insulating barrier between the probes and the InSb. The resistivity measurements were unsuccessful, but it was proved that the anodic oxide was electrically insulating as Bloom and Nemirovsky (1993:309) had stated was needed of a good passivant.

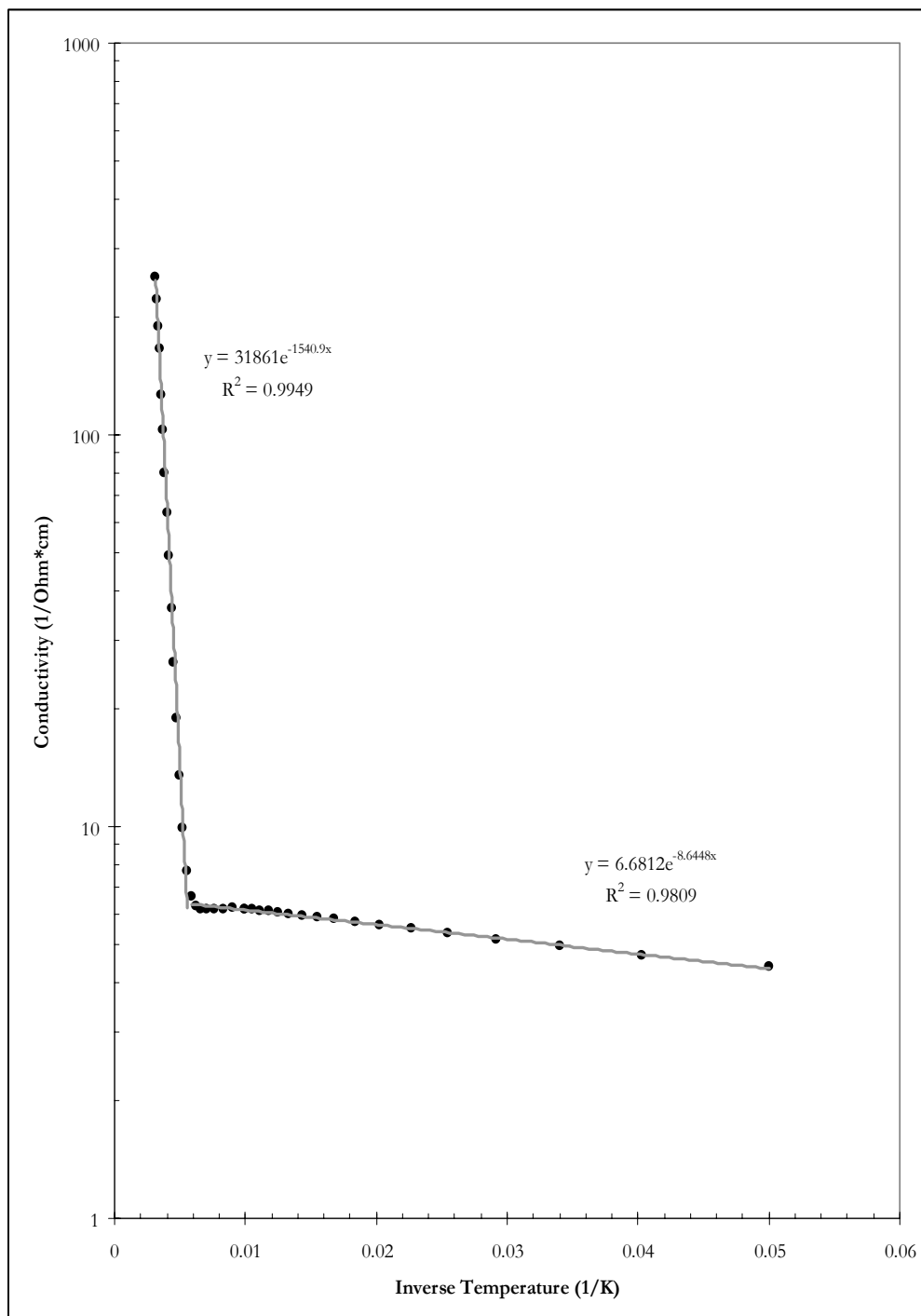


Figure 4.20. Conductivity of the SiO_x sample as a function of inverse temperature. The higher and lower temperature realms have been fitted with separate exponential curves.

4.5 Summary

Absorption and photoluminescence measurements were performed on bare InSb and InSb passivated with either anodic oxide or SiO_x . The bare InSb sample showed the existence of a radiative transition of 0.2322 eV at 22 K that shifted to 0.23145 eV at 24 K. The transition was unobservable above 24 K. Variable-temperature resistivity measurements showed activation energies at about 0.133 eV and 0.7 meV; the latter is thought to be due to shallow, effective-mass like donors.

V. Conclusions

5.1 Conclusions of Research

Activation energies of 0.133 eV and 0.7 meV were determined from variable-temperature resistivity measurements. The photoluminescent peak observed about 2 meV below the theoretical bandedge in the bare InSb sample is believed to be a real impurity level because it shifts with temperature and increases with increasing optical pump power.

5.2 Significance of Research

Photoluminescence is a valuable tool that can be used successfully to characterize passivated InSb. Results obtained by photoluminescence can be confirmed by both absorption and variable temperature resistivity measurements. However, the benefit of photoluminescence versus Hall measurements is that the photoluminescence is a contact-less measurement. Photoluminescence also has the capability to observe multiple activation energies that are close to each other, yet are not as apparent with the Hall measurements. This research showed promise of using an FT-IR spectrometer for the optical characterization of passivated InSb.

5.3 Recommendations for Future Research

Based on this research, we cannot make a recommendation at this time to L3 Communications: Cincinnati Electronics. This research shows promise, but, nevertheless, additional research is required. Further research is needed to investigate the cause of the photoluminescent peak ‘flipping’ and the unknown absorption/

photoluminescent peaks observed in the passivated samples that do not shift with temperature as would be expected for semiconductor energetic transitions.

Bibliography

- Advanced Research Systems. “Models LT-3-110 and LT-3B Helitran® Open Cycle Cryogenic Refrigeration System: Technical Manual.” 2001.
- Ashcroft, Neil W. & Mermin, N. David. *Solid State Physics*. United States: Brooks/Cole Thomson Learning, 1976.
- Bhattacharya, Pallab. *Semiconductor Optoelectronic Devices, 2nd Ed.* New Jersey: Prentice Hall 1993
- Bio-Rad Laboratories, Inc. “FTS/40A/60A: Getting Started Manual” 1992.
- Bloom, Ilan and Nemirovsky, Yael. “Quantum Efficiency and Crosstalk of an Improved Backside-Illuminated Indium Antimonide Focal-Plane Array,” *IEEE Transactions on Electron Devices*. Vol 38, No 8, 1991.
- “Surface Passivation of Backside-Illuminated Indium Antimonide Focal Plane Array,” *IEEE Transactions on Electron Devices*. Vol 40, No 2, 1993.
- Davis, Mike, Greiner, Mark, Sanders, John, and Wimmers, Jim. “Resolution issues in InSb focal plane array system design.” *SPIE Conference on Infrared Detectors and Focal Plane ArraysV, Orlando, FL, Conference 3379*. (Prepublication Copy) 1998.
- Del Mar Ventures. <http://www.sciner.com/Opticsland/ZnSe.htm> Accessed 2 March 2006.
- Dereniak, E.L. & Boreman , G.D. *Infrared Detection and Systems*. New York: John Wiley & Sons, Inc., 1996.
- Eisberg, Robert and Resnick, Robert. *Quantum Physics of Atoms, Molecules, Solids, Nuclei, and Particles, 2nd Ed.* New York: John Wiley & Sons, Inc., 1985.
- Haug, Hartmut and Koch, Stephan W. *Quantum Theory of the Optical and Electrical Properties of Semiconductors, 4th Ed.* New Jersey: World Scientific Publishing Co. Pte. Ltd. 2004.
- Hengehold, Robert L. “OENG 650: Optical Radiometry and Detection” Course Notes. AFIT/ENP 2004.
- Huang, Kerson. *Statistical Mechanics, 2nd Ed.* New York: John Wiley & Sons, 1987.

- Jaeger, Richard C. *Introduction to Microelectronic Fabrication*, 2nd Ed. New Jersey: Prentice-Hall, 2002.
- Long, Donald. *Energy Bands in Semiconductors*. New York: Interscience Publishers, 1968.
- Madelung, Otfried. *Semiconductors: Data Handbook*, 3rd Ed. New York: Springer, 2004.
- Mattausch, H.J. & Aspnes, D.E. "Optical properties of InSb and its electrochemically grown anodic oxide." *Physical Review B*, Vol. 23, No. 4, 1981.
- Moss, T. S. *Optical Properties of Semi-Conductors*. London: Butterworths Scientific Publications, 1959.
- Nussbaum, Allen & Phillips, Richard. *Contemporary Optics for Scientists and Engineers*. New Jersey, Prentice-Hall, Inc., 1976.
- O'Brian, Kevin & Witteborn, Fred C. "Thermal Contacts Between Metal and Glass for Use at Cryogenic Temperatures." *NASA Technical Memorandum 85856*. National Aeronautics and Space Administration: Ames Research Center, 1984.
- Pankove, J.I., *Optical Processes in Semiconductors*. New York: Dover Publications, Inc., 1971
- Saleh, B.E.A. & Teich, M.C. *Fundamentals of Photonics*. New York: John Wiley & Sons, Inc., 1991
- Sze, S.M. *Physics of Semiconductor Devices*. New York: John Wiley & Sons, 1981.
- *Semiconductor Devices: Physics and Technology*. New York: John, Wiley & Sons, 2002.
- Rogalski, Antoni, Adamiec, Krzysztof, & Rutkowski, Jarosław. *Narrow-Gap Semiconductor Photodiodes*. Bellingham, Washington: SPIE Press, 2000.
- Rode, D.L. "Electron Transport in InSb, InAs, and InP." *Physical Review B*, Vol 3, No 10, 1971.
- Willardson, R.K. and Beer, Albert C. *Semiconductors and Semimetals, Vol. 3: Optical Properties of III-V Compounds*. New York: Academic Press, 1967.
- Wilmsen, Carl W. *Physics and Chemistry of III-V Compound Semiconductor Interfaces*. New York: Plenum Press, 1985.

REPORT DOCUMENTATION PAGE				Form Approved OMB No. 074-0188	
<p>The public reporting burden for this collection of information is estimated to average 1 hour per response, including the time for reviewing instructions, searching existing data sources, gathering and maintaining the data needed, and completing and reviewing the collection of information. Send comments regarding this burden estimate or any other aspect of the collection of information, including suggestions for reducing this burden to Department of Defense, Washington Headquarters Services, Directorate for Information Operations and Reports (0704-0188), 1215 Jefferson Davis Highway, Suite 1204, Arlington, VA 22202-4302. Respondents should be aware that notwithstanding any other provision of law, no person shall be subject to a penalty for failing to comply with a collection of information if it does not display a currently valid OMB control number.</p> <p>PLEASE DO NOT RETURN YOUR FORM TO THE ABOVE ADDRESS.</p>					
1. REPORT DATE (DD-MM-YYYY) 13 June 2003		2. REPORT TYPE Master's Thesis		3. DATES COVERED (From – To) June 2003 – June 2006	
4. TITLE AND SUBTITLE CHARACTERIZATION OF PASSIVATED INDIUM ANTIMONIDE				5a. CONTRACT NUMBER	
				5b. GRANT NUMBER	
				5c. PROGRAM ELEMENT NUMBER	
6. AUTHOR(S) Taylor, Catherine Ann, BS, MS				5d. PROJECT NUMBER	
				5e. TASK NUMBER	
				5f. WORK UNIT NUMBER	
7. PERFORMING ORGANIZATION NAMES(S) AND ADDRESS(S) Air Force Institute of Technology Graduate School of Engineering and Management (AFIT/EN) 2950 Hobson Way WPAFB OH 45433-7765				8. PERFORMING ORGANIZATION REPORT NUMBER AFIT/GEO/ENP/06-03	
9. SPONSORING/MONITORING AGENCY NAME(S) AND ADDRESS(ES) N/A				10. SPONSOR/MONITOR'S ACRONYM(S)	
				11. SPONSOR/MONITOR'S REPORT NUMBER(S)	
12. DISTRIBUTION/AVAILABILITY STATEMENT APPROVED FOR PUBLIC RELEASE; DISTRIBUTION UNLIMITED					
13. SUPPLEMENTARY NOTES					
14. ABSTRACT Infrared absorption and photoluminescence measurements have been used to optically characterize bulk-grown, 680 μm thick, indium antimonide (InSb), both as-grown and after passivation by either anodization or a 700 \AA layer of silicon oxide (SiO_x). Spectra were obtained using Fourier transform infrared (FT-IR) spectroscopy. Results include the effects of sample temperature in the range of 10 – 300 K and 4.636 μm laser pump power in the range of 28 mW to 1.43 W for the photoluminescence spectrum.					
15. SUBJECT TERMS Photoluminescence, Absorption, Indium Antimonide, Passivation					
16. SECURITY CLASSIFICATION OF:			17. LIMITATION OF ABSTRACT UU	18. NUMBER OF PAGES 87	19a. NAME OF RESPONSIBLE PERSON Dr. Michael A. Marciniak
a. REPORT U	b. ABSTRACT U	c. THIS PAGE U			19b. TELEPHONE NUMBER (Include area code) (937) 255-3636, ext 4529 (Michael.Marciniak@afit.edu)